HPV16-Expressing Tumors Release Multiple IL1 Ligands to Orchestrate Systemic Immunosuppression Whose Disruption Enables Efficacy of a Therapeutic Vaccine

Lecointre, Morgane; Guillot, Jérémy; Marcone, Rachel; Ozdoganlar, Dilara; Cayatte, Marjorie; Jaensson Gyllenbäck, Elin; Liberg, David; Fournier, Nadine; Homicsko, Krisztian; Hanahan, Douglas

How to cite

LECOINTRE, Morgane et al. HPV16-Expressing Tumors Release Multiple IL1 Ligands to Orchestrate Systemic Immunosuppression Whose Disruption Enables Efficacy of a Therapeutic Vaccine. In: Cancer discovery, 2025, vol. 15, n° 7, p. 1458–1483. doi: 10.1158/2159-8290.CD-25-0382

This publication URL: https://archive-ouverte.unige.ch/unige:191423

Publication DOI: 10.1158/2159-8290.CD-25-0382

RESEARCH ARTICLE

HPV16-Expressing Tumors Release Multiple IL1 Ligands to Orchestrate Systemic Immunosuppression Whose Disruption Enables Efficacy of a Therapeutic Vaccine

Morgane Lecointre[1,2,3], Jérémy Guillot[1,2,3], Rachel Marcone[3,4], Dilara Ozdoganlar[1,2,3], Marjorie Cayatte[1,2,3], Elin Jaensson Gyllenbäck[5], David Liberg[5], Nadine Fournier[3,4], Krisztian Homicsko[1,2,3,6,7], and Douglas Hanahan[1,2,3,8]

ABSTRACT It is well-established that symptomatic cancers evade immune destruction by coalescing tumor microenvironments to suppress adaptive immunity. Additionally, mouse models of cervical and other cancers have revealed a capability of tumors to systemically induce the expansion of neutrophils that cripple T-cell development in spleen and lymph nodes, further impairing immune responses. Now we show that human papillomavirus type 16 (HPV16)–driven squamous cell tumors in the cervix and skin release into the circulatory system four immunoregulatory ligands – IL-1α, IL-1β, IL-33, and IL-36β – that bias the bone marrow toward granulocytic myelopoiesis, producing immunosuppressive neutrophils populating spleens and tumors. An IL-1 family coreceptor antagonist, anti-IL1RAP, abrogates this neutrophil expansion and complements an otherwise inefficacious HPV16 E7 peptide vaccine to elicit an effective antitumor immune response that is further sustained by anti–CTLA-4. Evidence for similarly IL-1–driven systemic immunosuppression in human cervical tumors encourages evaluation of this combinatorial therapeutic strategy for treating a largely immunoevasive cancer type.

SIGNIFICANCE: Cervical cancer is the fourth leading cause of cancer deaths in women worldwide. Although the disease is driven by two antigenic viral oncoproteins, therapeutic vaccines have proved ineffective, inferentially due to systemic immunosuppression. This study elucidated an actionable mechanism, whose disruption renders an oncoprotein vaccine efficacious, with translational potential.

INTRODUCTION

The immunobiology and immunotherapy of cancer are transcendent dimensions of basic and translational cancer research, with myriad complexities reflecting diverse regulation and dichotomous responses of the innate and adaptive immune systems. It is well-established that tumors establish multifaceted immunosuppressive microenvironments that are implicated in the variable efficacy of checkpoint inhibitors and other immunotherapies across the spectrum of human cancer types (1), involving in part innate immune cells, principally tumor-associated macrophages (TAMs) and neutrophils (TANs; refs. 1–5). Moreover, the abundance of circulating neutrophils, commonly scored as the blood neutrophil-to-lymphocyte ratio (NLR), is used clinically as a prognostic marker that is often associated with a worse prognosis for patients (6). In addition to immunosuppressive tumor microenvironments (TME), it has become evident that some tumors can elicit "systemic immunosuppression" (SIS), whereby the lymphoid organs are programmed to restrict the development of T-cell–mediated antitumor immunity (7). In addition to descriptive clues from patients with cancer, mouse models of human cancer have clearly established the existence of SIS. One example of SIS involves a genetically engineered mouse model (GEMM) of HPV16-induced squamous cell carcinomas (SCC) of the cervix and skin, in which we have reported a marked expansion of immunosuppressive myeloid cells in spleen (SP) and lymph nodes that inhibit the development of tumor antigen–specific T cells and render a potent HPV16 E7 peptide vaccine ineffacious (8, 9). Indeed, the surprising failure of this therapeutic vaccine, targeting an antigenic oncoprotein involved in HPV16-driven carcinogenesis, led us to appreciate the importance of SIS as a means of evading immune destruction, and to elucidate its mechanism and means to abrogate it, so as to enable vaccines and other immunotherapies against cervical cancer. Other concurrent reports similarly describe SIS in mouse models of breast, colon, melanoma, and lung cancers (10, 11). Whereas these studies provided clues into the induction and manifestation of myeloid expansion and consequent SIS, the regulatory mechanisms governing SIS have remained elusive. Herein, we report a comprehensive evaluation of SIS in cervical cancers in a mouse model and in humans. We present data implicating the expression in tumors and release into the circulation of four members of the IL-1 superfamily of cytokine ligands, which act concertedly to program the biased development and aberrant expansion of immunosuppressive neutrophils in bone marrow (BM) and SP, and in tumors, whose collective importance is revealed by pharmacologic coinhibition of their distinctive receptors, which unlocks the latent benefits of a therapeutic vaccine, producing remarkable combinatorial efficacy.

[1]Swiss Institute for Experimental Cancer Research (ISREC), EPFL, Lausanne, Switzerland. [2]Swiss Cancer Center Leman (SCCL), Lausanne, Switzerland. [3]Agora Translational Cancer Research Center, Lausanne, Switzerland. [4]Bioinformatics Core Facility, Swiss Institute of Bioinformatics (SIB), Lausanne, Switzerland. [5]Cantargia AB, Lund, Sweden. [6]Department of Oncology, CHUV, Lausanne, Switzerland. [7]Center for Personalized Oncology, CHUV, Lausanne, Switzerland. [8]Ludwig Institute for Cancer Research, Lausanne, Switzerland.

M. Lecointre and J. Guillot contributed equally to this article.

Corresponding Author: Douglas Hanahan, Agora Translational Cancer Research Center, Rue du Bugnon 25A, Lausanne CH-1011, Vaud, Switzerland. E-mail: douglas.hanahan@epfl.ch

Cancer Discov 2025;15:1458–83

doi: 10.1158/2159-8290.CD-25-0382

RESULTS

Systemic Expansion of Immunosuppressive Neutrophils during Squamous Cell Carcinogenesis

This study focused upon the K14HPV16/H2b mouse model, which expresses the HPV16 early region oncogenes under control of the human K14 promoter in FVBN mice congenic for the H2b MHC locus. Female mice develop cervical SCC by 5 months of age via cervical epithelial neoplasias (CIN1–3) in the context of sustained, physiologic levels of estrogen (E_2; ref. 9). Reflecting the additional expression of the E6 and E7 oncoproteins in basal (K14-expressing) keratinocytes, both male and female mice also progressively develop epidermal neoplasias, and eventually (6–12 months), SCCs that are similar to HPV16-driven human head and neck SCC (HNSC). Both males and females with squamous neoplasias and carcinomas manifest SIS (9). An earlier generation of this model in the FVBN/H2q background has been widely used to study the parameters of cervical and epidermal squamous cell carcinogenesis, their similarities to the cognate human cancers, and responses to therapeutic targeting (12–18). Notably, the H2q haplotype of the first-generation model does not present peptides from the E6 or E7 oncoproteins on class I MHC to CD8 T cells (9, 19), and there is no evidence for immune evasion (20), motivating the development (described in ref. 9) of a second-generation K14HPV16 transgenic mouse model that is inbred for FVBN, which is permissive for squamous cell carcinogenesis, but also congenic for the H2b MHC locus, which presents E6/E7 peptides on class I MHC, thus enabling evaluation of HPV16 oncoprotein-based vaccines.

Aiming to more thoroughly characterize the SIS phenotype and to illuminate the mechanisms underlying its induction during HPV16-induced squamous carcinogenesis, we performed single-cell RNA sequencing (scRNA-seq) on key organs. For the early stages of tumor development, we comparatively analyzed – from FVBN/H2b (control) and K14HPV16/H2b mice – normal or dysplastic ear skin, BM, SP, and blood from the same mice. We included BM due to its role in myeloid cell development, further incentivized by our observation that the hematopoietic lineage in K14HPV16/H2b mice is altered and biased toward granulocytic cell development (Supplementary Fig. S1A and S1B). Finally, cervical carcinomas were used for the late stage of tumor development.

We first focused on neoplastic development in the comparatively accessible epidermis. The scRNA-seq data revealed the recruitment of neutrophils to dysplastic skin (Fig. 1A and B) along with an increase in neutrophil abundance in BM, SP, and blood (Fig. 1C; Supplementary Fig. S1C and S1D). Seeking to understand how HPV16-transformed basal keratinocytes modify neutrophil differentiation, we applied the neutrotime transcriptional signature (24), which describes the developmental spectrum of neutrophils spanning BM, blood, and SP, ordered chronologically. Differential expression of key neutrotime biomarkers allowed us to identify three periphery-associated neutrophil (PAN) subclasses in mice with skin dysplasia, namely precursor neutrophils that we designated as prePAN, as well as early and late developmental stages, called PAN-1 and PAN-2, respectively (Fig. 1D; Supplementary Fig. S1E). Next, we used the neutrotime signature to score their chronologic development and abundance, which revealed that prePAN, PAN-1, and PAN-2 were all highly represented in the BM, whereas blood and SP were predominantly comprised of the PAN-2 subset (Fig. 1E; Supplementary Fig. S1F).

We next assessed neutrophil phenotypes by applying a "myeloid-derived supressor cell (MDSC)"–specific mRNA signature for immunosuppressive myeloid cells of the granulocytic and monocytic lineages (25, 26). The PAN-2 subclass in dysplastic K14HPV16/H2b mice had the highest MDSC score, which was significantly increased compared with PAN-2 in control nontransgenic H2b counterparts and to prePAN and PAN-1 in both backgrounds (Fig. 1F). *Ex vivo* coculture of CD8 T cells with total myeloid cells (CD11b) or purified neutrophils isolated from SPs of K14HPV16/H2b mice confirmed the suppressive nature of these cells (in contrast to H2b mice), as shown by the decreased capacity of CD8 T cells to proliferate (Fig. 1G). Collectively, these data reveal that the premalignant stages of HPV16 tumor development elicit SIS that is associated with an expansion of immunosuppressive neutrophils in BM, SP, and blood.

Mirroring the premalignant phenotype, cervical tumor–bearing mice (K14HPV16/H2b-E_2) also had an expansion of PAN-2 cells associated with SIS (Supplementary Fig. S1G), along with myeloid infiltration in the TME, primarily consisting of TANs, concomitant with minimal lymphocyte infiltration (Fig. 1H and I). Cluster analysis of neutrophils in the TME identified two putative subtypes (Supplementary Fig. S1H). We further characterized neutrophils along their development stages by comparing the two TAN clusters (1 and 2) with the PAN-2 subtype found in the blood (Fig. 1J). Using a pseudotime analysis, we identified a continuum of differentiation followed by neutrophils arriving from the periphery upon entering the TME (Fig. 1K). Applying activity signatures, we observed that blood-borne PAN-2 infiltrating the tumor differentiate into a population of neutrophils exhibiting a high MDSC signature score (TAN-1), as well as another (TAN-2) exhibiting a signature representative of a long-lived tumor-promoting neutrophil population variously known as N5 (27) or Siglec-F^{high} (Fig. 1L; Supplementary Fig. S1I; ref. 28). Concordantly, scRNA-seq data analysis of human cervical cancer (CESC) infiltrated with neutrophils (Fig. 1M) established the presence of TANs positive for the MDSC (hTAN-1) and N5 (hTAN-2) signature scores, reinforcing the relevance of our GEMM (Fig. 1N and O). For logistical reasons we have been unable to evaluate the first-generation H2q-based models of skin and cervical cancers for evidence of neutrophil expansion and SIS in BM and SP; TAMs and TANs have been studied previously in these models, principally in regard to the angiogenic phenotype (15–18, 29–31), and their immunosuppressive phenotypes have not been evaluated.

Implicating the IL-1 Superfamily in Induction of SIS

Seeking to clarify interactions underlying SIS in our GEMM, we next applied the CellChat algorithm (32) to interrogate cross-organ communication between the TME and the periphery, which implicated cancer cells as the principal cell population in the TME with the potential to interact with neutrophils in the BM and SP (Fig. 2A). In particular, cancer cells were

predicted to preferentially interact with PAN-2 neutrophils. Moreover, TANs were inferred to participate in the communication at a distance with peripheral neutrophils in the BM and SP, suggesting these cells may sustain or amplify SIS once recruited into the TME.

Based on this interaction model, we hypothesized that cross-organ communication should be mediated by circulating soluble factors produced by HPV16-affected tissues and released into the bloodstream to act at a distance on neutrophil differentiation in myeloid cell reservoirs. To test this hypothesis, we performed a colony-forming unit (CFU) assay, optimized for the growth of myeloid progenitors, using BM hematopoietic stem and progenitor cells (HSPC; Supplementary Fig. S2A). In line with our previous observations, more colonies were obtained for HPV HSPCs, with an increased proportion of granulocyte CFUs (CFU-G) compared with H2b controls, indicative of elevated granulopoeisis in the GEMM (Supplementary Fig. S2B and S2C). Interestingly, control HSPCs preincubated with serum from K14HPV16/H2b mice with skin dysplasias fully recapitulated the HPV16 CFU profile, whereas cells preincubated with H2b serum did not (Supplementary Fig. S2C). These results implicate soluble factors in K14HPV16/H2b serum that can influence neutrophil differentiation, potentially leading to the induction of SIS.

To identify candidates for this effect, we used a multiomics-based interactome approach. We conducted a proteomic analysis and used a quantitative cytokine array to identify soluble factors enriched in the blood of K14HPV16/H2b mice. Using our scRNA-seq datasets, we next selected ligands expressed in dysplastic and tumor tissues, for which cognate receptors were expressed in the BM and SP (Fig. 2B). This cross-organ analysis led to the identification of 93 candidates (Supplementary Table S1), among which 50 ligands had the potential to interact preferentially with neutrophils in both the BM and SP (Supplementary Fig. S2D; Supplementary Table S1).

In parallel, we derived three cancer cell lines from spontaneous SCCs of the epidermis arising in the K14-HPV16/H2b GEMM, which exhibited distinctive phenotypes upon inoculation subcutaneously into the flank of H2b control mice (Fig. 2C; Supplementary Fig. S2E–S2G). We identified one "immunosuppressive" cell line, called H16sc-IS1, which recapitulated the phenotype observed in the K14HPV16/H2b GEMM by inducing myeloid expansion in the BM, leading to T-cell–immunosuppressive neutrophils in SP and the TME, and preferentially recruiting neutrophils (including Siglec-F$^+$ TANs) into the TME (Fig. 2D and E; Supplementary Fig. S2F–S2H). A second, the "immunopermissive" cell line H16sc-ImP, did not induce SIS and formed tumors primarily infiltrated by non-immunosuppressive macrophages (Fig. 2E; Supplementary Fig. S2G). The third "intermediate" cell line H16sc-Int recruited both neutrophils and macrophages into the TME but failed to induce a robust SIS (Supplementary Fig. S2F and S2G). These three cell lines, all derived from primary GEMM tumors, likely reflect the intratumoral heterogeneity of tumors arising via multistage tumorigenesis, with some cancer cell clones displaying an H16sc-IS1 phenotype, whereas others may display H16sc-ImP or H16sc-Int phenotypes, which could explain the increased abundance of tumor-infiltrating neutrophils in pure H16sc-IS1 tumors compared with the GEMM. This observation deserves future investigation.

Seeking to refine our list of 93 candidate inducers of SIS, we reasoned that key soluble factors should be shared by our GEMM and H16sc-IS1–derived tumors while being absent or expressed to a lower extent in the H16sc-Int– and H16sc-ImP–derived tumors. Therefore, we extracted total RNA from similarly sized tumors arising from transplantation of the three cell lines and assessed expression of the 93 ligands. Notably, the three cell line–derived tumors had distinctive expression patterns (Fig. 2F). Amongst the initial 93 candidates, 44 ligands were specifically enriched in H16sc-IS1 tumors, of which 27 could potentially interact with neutrophils via expressed cognate receptors (Fig. 2G and H; Supplementary Table S1). Within this refined list of candidates (Fig. 2H), we found chemokines well known to attract neutrophils, such as CXCL1 and CXCL5, and proteins involved in cell adhesion processes, collectively required for neutrophil mobilization rather than their generation (33–35). As expected, the growth factor G-CSF/CSF3, which is involved in stimulating neutrophil production, was also present (36). Strikingly, nearly half of the IL-1 cytokine superfamily (IL-1α, IL-1β, IL-1RA, IL-33, and IL-36β) were part of the refined set of 27 candidates, suggesting these cytokines could be involved in the induction of SIS.

We next assessed the relevance of these factors for human cervical cancer. We interrogated the SAveRUNNER drug repurposing prediction tool in the context of human CIN (37). Congruently, two molecules targeting the IL-1 pathway ranked in the top 10 most promising drugs, ahead of molecules currently used in the clinic to treat patients with cervical cancer (Supplementary Fig. S2I). More specifically, a trap protein acting as a soluble decoy receptor for both IL-1α and IL-1β ranked number 2, before an anti–IL-1β mAb (38, 39).

Taken together, these data raise the hypothesis that members of the IL-1 cytokine superfamily, particularly IL-1α and IL-1β, interact with neutrophils in the BM and SP so as to induce SIS. Notably, in addition to IL-1α and IL-1β, circulating protein levels of IL-33 and IL-36β were also found to be highly enriched in H16sc-IS1 tumor–bearing mice and in the GEMM, suggesting that they too could be involved (Supplementary Fig. S2J).

We next used the NicheNet algorithm to explore this hypothesis, as it can predict interactions between a ligand and receiver cells based on downstream pathway activation (40). We asked whether *Il1a*, *Il1b*, *Il33*, and *Il36b* were associated with pathway activation of their cognate receptors in peripheral myeloid cells using *Csf3* as a reference. As expected, *Csf3* was predicted to strongly interact with and activate BM and SP neutrophils (Fig. 2I). In the BM, *Il1a*, *Il1b*, *Il33*, and *Il36b* had similar inferred interactions with prePANs compared with *Csf3*. Strikingly, however, the IL-1 ligands all had stronger predicted biological effects on the PAN-1 (BM) and PAN-2 (BM and SP) subsets than *Csf3*, suggesting that these four IL-1 superfamily members are attractive SIS-inducing candidates. Motivated by these data, we next aimed to address the question of their necessity and sufficiency for SIS induction.

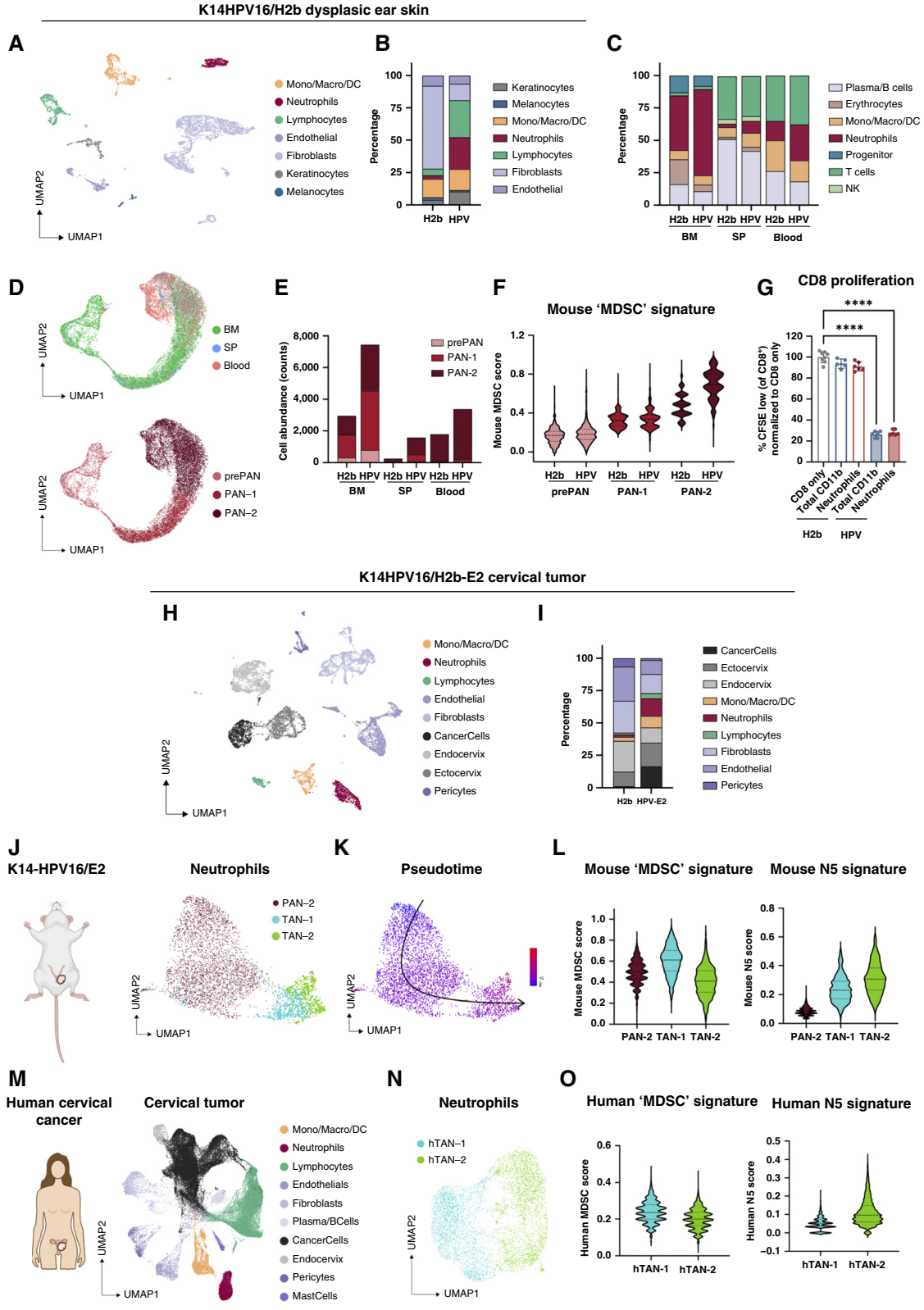

Figure 1. Immunosuppressive neutrophils are systemically expanded during squamous cell carcinogenesis in K14HPV16/H2b (HPV) mice. **A,** UMAP projection of major cell types from healthy ear skin (H2b) and dysplastic ear skin lesions (HPV) combined. **B** and **C,** Relative cell type abundance (percentage) in ear skin (**B**) and in BM, SP, and blood (**C**) from H2b vs. HPV mice. **D,** UMAP projection of neutrophils from BM, SP, and blood, labeled by organ (top) and developmental stages (bottom) based on the neutrotime score. **E,** Abundance of neutrophil developmental stages (counts) in BM, SP, and blood from H2b vs. HPV mice. **F,** MDSC signature score in neutrophils from H2b and HPV mice for each developmental stage. (*continued on following page*)

Characterizing the Induction of SIS by IL-1 Superfamily Ligands

We next performed a time-course experiment, analyzing peripheral myeloid and neutrophil expansion during tumor growth as well as their capacity to suppress CD8 T-cell activity. Tissue samples from H16sc-IS1 tumor–bearing mice were collected at different tumor volumes (Fig. 3A). Continuing growth from nascent tumors (25–50 mm^3) was associated with a progressive accumulation of myeloid cells and neutrophils in the SP (Fig. 3B, right *Y*-axis). Furthermore, coculture of activated CD8 T cells and CD11b cells from the SP revealed a correlation between myeloid accumulation during tumor growth and impaired CD8 proliferation, leading to phenotypic SIS beginning at tumor volumes >80 mm^3 (Fig. 3B, left *Y*-axis).

Among the IL-1 cytokine superfamily candidates, whereas IL-33 and IL-36β bind selectively to their own receptors, IL-1α and IL-1β share the same receptor (Supplementary Fig. S3A). Notably, in the K14HPV16/H2b mouse model, *Il1b* is exclusively expressed by myeloid cells, especially neutrophils, and not cancer cells, suggesting that it could be involved in maintaining or amplifying myeloid expansion rather than in initial SIS induction by cancer cells (Supplementary Fig. S3B). Using the RNAscope technology, we confirmed that *Il1a*, *Il33*, and *Il36b* are expressed in cancer cells in H16sc-IS1 tumors (Supplementary Fig. S3C). Aiming to elucidate the induction of SIS by cancer cells, we chose to focus our investigation on the role of IL-1α rather than IL-1β.

We began by analyzing the serum content of the candidate ligands as a function of SP size normalized by body weight, which mirrors the myeloid accumulation (Supplementary Fig. S3D). IL-1α and IL-36β concentrations positively correlated with the SP enlargement (Fig. 3C), in contrast to G-CSF and IL-33, which did not (Supplementary Fig. S3E). Furthermore, expression levels in nascent tumors of *Il1a*, *Il33*, and *Il36b* but not *Csf3* mRNAs positively correlated with peripheral myeloid cell suppressiveness toward CD8 T cells (Supplementary Fig. S3F), reinforcing the postulated role of these factors in the induction of SIS.

To test this hypothesis, we used Hoxb8 cells, a mouse neutrophil progenitor cell line conditionally immortalized in the presence of tamoxifen. Upon tamoxifen removal, Hoxb8 cells were treated with various cytokine regimens as they were differentiating into neutrophils (Supplementary Fig. S3G). Interestingly, whereas treatment with individual IL-1 superfamily ligands did not affect MDSC marker gene expression compared with G-CSF, each in combination with G-CSF induced a strong response characterized by different profiles of MDSC marker gene expression (Supplementary Fig. S3H). When the three IL-1 superfamily ligands were combined with G-CSF, the response was distinct from any of their individual combinations with G-CSF (Supplementary Fig. S3H), indicating that these three molecules induce overlapping but not identical downstream effects.

Moving to *in vivo* experiments, a deconvolution study was performed by systemically administering individual ILs or the combination of the three ILs in H2b control mice compared with G-CSF alone. Mice received four rounds of intraperitoneal injection (every 2-3 days) before SPs were collected. In contrast to the *in vitro* results with the Hoxb8 system, IL-1α alone was more potent than G-CSF, inducing a more extensive neutrophil expansion in the SP and generating more suppressive myeloid cells (Fig. 3D and E). Moreover, addition of IL-33 and IL-36β potentiated the IL-1α effects, inducing a further expansion of myeloid cells – principally neutrophils – in the SP (Fig. 3D), and these myeloid cells were potently suppressive of CD8 T cells (Fig. 3E). We then sought to explain the discrepancy between the *in vitro* and *in vivo* experiments. Knowing that IL-1 pathway activation may stimulate G-CSF production, we hypothesized that intraperitoneal inoculation of IL-1α into mice would increase G-CSF levels in the blood circulation, thus obviating the need to supply exogenous G-CSF. We therefore quantified G-CSF in the serum of treated mice, and indeed, G-CSF was markedly induced in mice that had received either IL-1α or the triplet-IL regimen (Fig. 3F). Moreover, combining the three ILs with G-CSF further exacerbated the SIS phenotype in H2b control mice, indicative of their cooperativity (Supplementary Fig. S3I–S3K).

We proceeded to confirm these data in tumor-bearing mice. To do so, we engineered the H16sc-ImP cell line, which does not induce SIS, to overexpress (OE) *Il1a*, *Il33*, and *Il36b* (triplet-IL). Upon inoculation into syngeneic mice, triplet-IL-OE H16sc-ImP tumors grew faster, concomitant with SP enlargement (Fig. 3G and H). Once again, the SP enlargement mirrored systemic myeloid and neutrophil expansion in the BM and SP (Fig. 3I). We characterized the serum content and, much as for H16sc-IS1 tumors, IL-1α and IL-36β concentrations were increased and correlated with the SP size normalized to body weight (Fig. 3J; Supplementary Fig. S3L). Moreover, in line with cytokine inoculation into normal mice, triplet-IL-OE H16sc-ImP cells induced expression and secretion of G-CSF into the conditioned media of cultured cells (Supplementary Fig. S3M and S3N), which was increased in the serum of tumor-bearing mice (Fig. 3J). To further the characterization, we performed a time-course analysis (Fig. 3K). Congruent with the H16sc-IS1 results (Fig. 3B), myeloid and neutrophil expansion began in nascent tumors, and these cells were capable of suppressing CD8 T cells, in contrast to the parental cells that were not overexpressing the three ILs (Fig. 3K). Well-established SIS

Figure 1. ***(Continued)*** Scores were compared with the Welsh two-sample *t* test: $P = 7.61e{-}05$ (prePAN), $P = 9.82e{-}14$ (PAN-1), and $P < 2.2e{-}16$ (PAN-2). For **A**–**F**: $n = 3$ per organ and condition (H2b or HPV). **G,** *In vitro* proliferation assay of anti-CD3/anti-CD28–activated CD8 T cells cocultured with CD11b cells or neutrophils isolated from the SP of H2b ($n = 5$–6) and HPV mice ($n = 5$–6). Data are shown as the mean ± SD, statistical analysis by the Kruskal–Wallis test, ****, $P < 0.0001$. **H,** UMAP projections of major cell types in K14HPV16/H2b-E_2 (HPV-E_2) cervical tumors and healthy cervix (H2b) combined. **I,** Relative cell type abundance (percentage) in cervical tumors (HPV-E_2) and healthy cervix (H2b). **J,** UMAP projection with neutrophils from the blood (HPV) and cervical tumors (HPV-E_2) labeled by the major clusters PAN-2, TAN-1, and TAN-2. **K,** Pseudotime analysis of neutrophils from the blood (HPV) and cervical tumors (HPV-E_2). **L,** MDSC and N5 signature scores in neutrophils from the blood (HPV) and mouse cervical tumors (HPV-E_2). Signature scores were compared between the TAN-1 and TAN-2 populations with paired *t* tests: $P = 8.96e{-}04$ (MDSC score), $P = 0.010$ (N5 score). For **H**–**L**: $n = 3$ per organ and condition (H2b, HPV or HPV-E_2). For **M**–**O**: scRNA-seq data of human cervical tumors ($n = 12$) were reanalyzed from Guo and colleagues (21), Dai and colleagues (22), and Li and colleagues (23). **M,** UMAP projection of major cell types in human cervical tumors. **N,** UMAP projection of the two human TAN subtypes, hTAN-1 and hTAN-2. **O,** MDSC and N5 signature scores in the human TAN subtypes. Signature scores were compared between the hTAN-1 and hTAN-2 populations with paired *t* tests: $P = 4.61e{-}04$ (MDSC score), $P = 0.0011$ (N5 score). DC, dendritic cell.

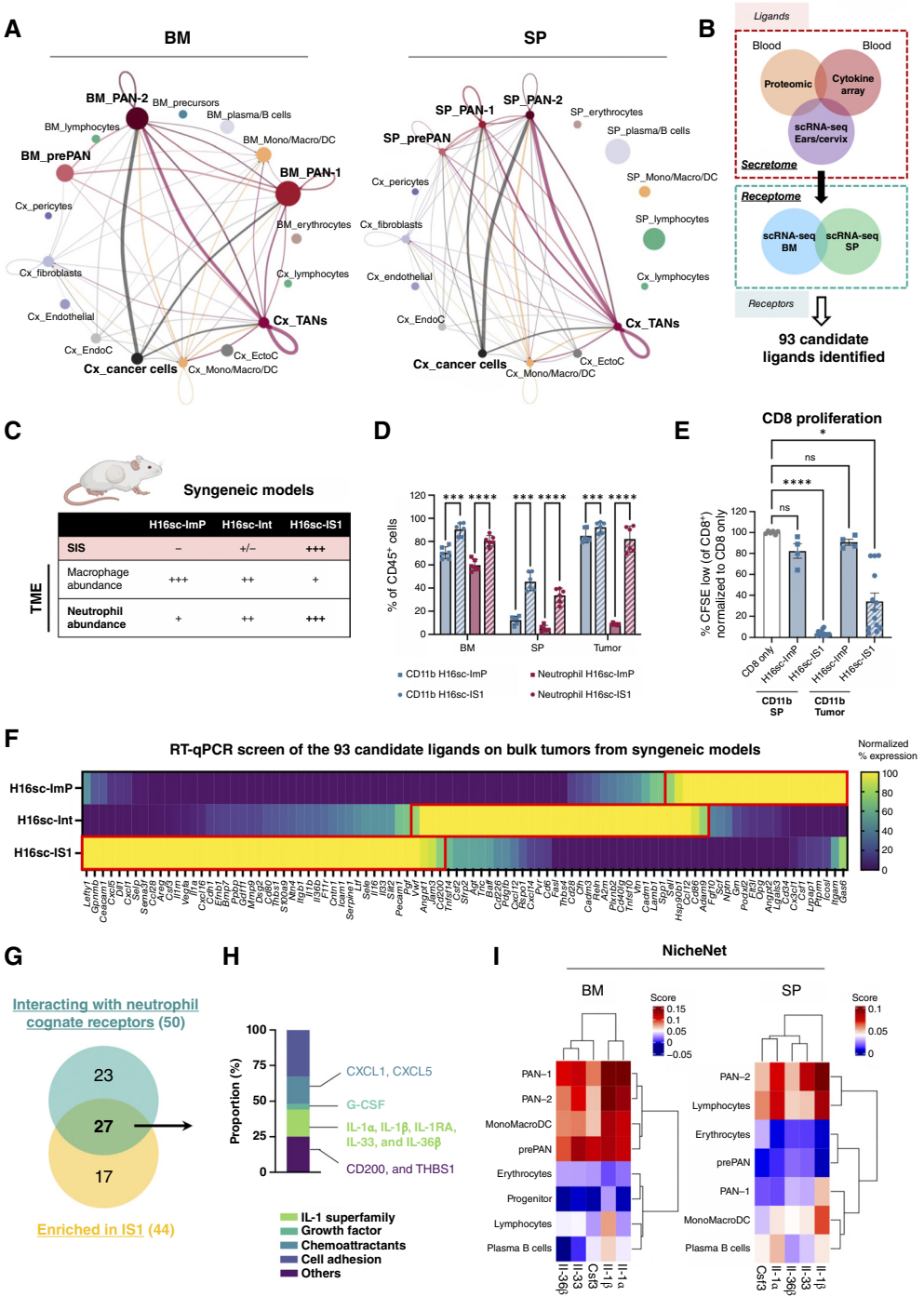

Figure 2. Identification of candidate SIS-inducing ligands. **A,** Cell–cell communication inferred from secreted signaling molecules expressed in cervix to receptors expressed in BM cells (left) or SP cells (right). Line thicknesses represent probabilities of communication. **B,** Schematic of interactome analysis for candidate ligand identification. Soluble factors enriched in serum are integrated with scRNA-seq data from lesional tissues, BM, and SP. **C,** Summary table of SIS status and tumor myeloid cell composition in three syngeneic tumor models based on GEMM-derived cancer cell lines. **D,** Quantification by flow cytometry of total myeloid cells (CD11b$^+$) and neutrophils (CD11b$^+$; Ly6G$^+$) in BM, SPs, and tumors of H16sc-ImP ($n = 6$) and H16sc-IS1 ($n = 6$) mice. Data are shown as the mean ± SD. **E,** *In vitro* proliferation assay of anti-CD3/anti-CD28–activated CD8 T cells cocultured with CD11b$^+$ cells isolated from the SPs and tumors of H16sc-ImP ($n = 4$) and H16sc-IS1 ($n = 13$) mice. **F,** Normalized gene expression of the 93 candidate ligands, measured by RT-qPCR analysis of bulk tumors from the three distinctive syngeneic tumor models ($n = 3$ per model). **G,** Intersection between ligands enriched in the H16sc-IS1 model and the 93-candidate–associated cognate receptors preferentially expressed in neutrophils. **H,** Proportion of selected ligands among the reduced list of 27 candidates. **I,** NicheNet scores obtained for particular ligands (*Il1a*, *Il1b*, *Il33*, *Il36b*, and *Csf3*) based on differentially expressed genes between HPV and H2b mice in each cell population of BM (left) and SP (right). Data in quantitative panels are presented as the mean ± SEM, unless specified otherwise. (*, $P < 0.05$; **, $P < 0.01$; ***, $P < 0.001$; ****, $P < 0.0001$; ns, no statistical significance; computed with the two-way ANOVA or Kruskal–Wallis test). DC, dendritic cell.

was observed by ~150 mm^3, with an immune profile in the SP replicating that of H16sc-IS1 tumor–bearing mice (Fig. 3L). Moving on to the TME, triplet-IL overexpression also markedly altered the TME, leading to expansive myeloid infiltration, mostly involving neutrophils, resulting in a similar profile to the TME of H16sc-IS1–derived tumors (Fig. 3M–O). Collectively, these data attest to the functional role of the three ILs, and of the G-CSF they induce, during the manifestation of SIS.

Assessing the IL-1 Superfamily in Human Cervical Cancer

We next investigated the involvement of the IL-1 cytokine superfamily in human cervical cancer. To do so, we first defined an SIS gene signature. To independently identify genes selectively associated with IL-1–induced SIS, we utilized the triplet-IL-OE H16sc-ImP and the otherwise isogenic Ctrl H16sc-ImP cancer cell lines overexpressing or not the IL-1 triplet (*Il1a*, *Il33*, and *Il36b*). After performing comparative transcriptome profiling using RNA-seq (Supplementary Table S2), we focused on the top 200 most upregulated genes in triplet-IL-OE H16sc-ImP cells, which we integrated with the previously identified 93 candidate ligands, producing an SIS signature of 10 genes, including *Il1a*, *Il33*, *Il36b*, *Csf3*, and *Cxcl2/5* (Fig. 4A and B). These data suggest that IL-1 superfamily signaling is an upstream regulator of other genes encoding key proteins involved in communication and recruitment of neutrophils, such as G-CSF/CSF3 and CXCL2/5. We first quantified most of these factors in the serum of patients with cervical cancer. Interestingly, their concentrations increased with the tumor stage, suggesting potential utility as SIS biomarkers (Supplementary Fig. S4A). We next applied this SIS signature to the CESC dataset in The Cancer Genome Atlas (TCGA) and observed an association with worse survival (Fig. 4C) as well as a positive correlation with neutrophil infiltration (Fig. 4D), suggesting that CESC might be modulated by neutrophil-mediated SIS induced by the triplet combination of IL-1α, IL-33, and IL-36β.

We also assessed features of SIS in other cancer types by performing an unsupervised clustering analysis of patients in a TCGA dataset of 13 tumor types based on expression of the 93 candidate ligands identified above (Fig. 2B; Supplementary Table S1). Interestingly, most of the SIS signature genes, including *IL1A*, *IL1B*, *IL36B*, as well as other genes that were enriched in the SIS-inducing H16sc-IS1 tumor model (Fig. 2F), segregated together to define a hotspot of patients sharing common characteristics (Supplementary Fig. S4B). In addition to CESC, this hotspot included patients with HNSC, bladder cancer (BLCA), and lung SCC (LUSC), along with small proportions of patients with uterine corpus endometrial carcinoma (UCEC), lung adenocarcinoma (LUAD), and colorectal cancer (COAD and READ; Supplementary Fig. S4C). Interestingly, similarly to CESC, a high SIS score correlated with a worse survival probability and with increasing neutrophil infiltration in HNSC, BLCA, and LUSC, suggesting that pan–IL-1–induced neutrophil-mediated SIS may be operative beyond CESC (Supplementary Fig. S4D and S4E). Given our focus on the mechanisms of SIS and its role in the failure of therapeutic vaccines for CESC, these associations have not been further investigated.

Pharmacologic Inhibition of Pan–IL-1 Superfamily Signaling Disrupts Systemic Neutrophil Expansion

Having collectively implicated IL-1α, IL-33, and IL-36β in SIS induction, we hypothesized that cotargeting these cytokines should disrupt SIS. As previously mentioned, IL-1α, IL-33, and IL-36β signal through three distinct receptor complexes, which nevertheless share a common coreceptor, IL1RAP, which is necessary for downstream signaling (Supplementary Fig. S3A). Therefore, targeting this coreceptor represents an attractive therapeutic strategy. We first assessed *Il1rap* expression using scRNA-seq data from the GEMM (Supplementary Fig. S5A) and flow cytometry analyses from the H16sc-IS1 tumor model (Supplementary Fig. S5B). *Il1rap* proved to be predominantly expressed and upregulated in neutrophils in the BM, SP, and TME of tumor-bearing mice, whereas it was expressed at a much lower level in cancer cells. We also confirmed that *Il1rap* is highly expressed in human tumor neutrophils based on scRNA-seq data (Supplementary Fig. S5C). Although we assess possible effects on cancer cells below, these data suggest that targeting IL1RAP should mainly affect neutrophil populations in the periphery and the TME.

We therefore assessed in preclinical trials an anti-IL1RAP blocking antibody (mNadunolimab, clone 3A9) that is able to abrogate signaling mediated by IL-1α, IL-1β, IL-33, and IL-36; this antibody additionally serves as a mouse surrogate for nadunolimab (CAN04, Cantargia AB), a human-specific anti-IL1RAP antibody that is currently in clinical trials – unrelated to targeting neutrophils or SIS – for the treatment of different solid tumors.

Anti-IL1RAP treatment of H16sc-IS1 tumor–bearing mice that were spontaneously developing SIS (Fig. 5A) resulted in a delayed tumor growth compared with isotype control (IC)-treated mice (Fig. 5B), which was associated with a reduced SP size – a macroscopic readout for SIS – indicative of a peripheral response after treatment (Fig. 5C). We then analyzed the peripheral compartments, starting with the BM. We observed that SIS-associated myelopoiesis dysregulation was reversed under treatment, with a decreased proportion of GMPs (Fig. 5D), consistent with the reduced neutrophil abundance in the BM and SP observed by FACS on day 10 (Fig. 5E). To exclude the possibility that this effect could be driven by a difference in tumor burden following anti-IL1RAP therapy, we compared the SPs of anti-IL1RAP–treated mice with IC-treated mice bearing size-matched tumors and observed that the latter had significantly greater abundance of SIS-mediating splenic neutrophils (Supplementary Fig. S5D), confirming a tumor burden–independent effect of anti-IL1RAP therapy. In contrast to the periphery, no significant changes were observed in the TME (Supplementary Fig. S5E). Unsurprisingly, given the absence of IL1RAP expression in T cells (Supplementary Fig. S5A and S5B), anti-IL1RAP did not produce significant alterations to the lymphocyte compartment in the periphery or the TME (Supplementary Fig. S5F). Finally, anti-IL1RAP monotherapy reduced the NLR in the SP (Fig. 5F), which correlated with both SP size and blood NLR in H16sc-IS1 tumor–bearing mice (Supplementary Fig. S5G).

As noted above, the blood NLR is used clinically as a prognostic marker and is often associated with a worse prognosis for patients (6, 41). Therefore, we analyzed neutrophil and

lymphocyte counts as well as the NLR in the blood of patients with PDAC and NSCLC treated with nadunolimab monotherapy (CANFOUR trial, NCT03267316). Strikingly, treated patients presenting with a high neutrophil count at baseline had a progressive and significant decrease in circulating neutrophils from day 8 onward and in the blood NLR over time, reaching levels observed in patients with normal neutrophil counts at baseline (Fig. 5G). Thus, anti-IL1RAP monotherapy was able to normalize the blood NLR without inducing neutropenia in human patients with cancer. These data mirror our results in the mouse model, as well as a recent report assessing the effects of anti-IL1RAP in mouse and human PDAC (42).

We next considered whether the tumor growth delay observed upon anti-IL1RAP monotherapy could be partially explained by an effect of the treatment on cancer cells and not just on neutrophils. Multiple lines of investigation indicate that IL1RAP expression on cancer cells is not impactful. First, when the anti-IL1RAP antibody was added to H16sc-IS1 cancer cells, there was no effect on their proliferative capacity (Supplementary Fig. S5H). Second, when the expression of *Il1rap* mRNA was knocked-down with siRNAs, there was no effect on *Il1a*, *Il33*, *Il36b*, and *Csf3* gene expression nor expression of other genes important for neutrophil recruitment (Supplementary Fig. S5I). These results imply that blockade of IL1RAP in cancer cells was not affecting their secretome and therefore should not affect their communication at a distance with peripheral neutrophils. Finally, anti-IL1RAP therapy in the neutrophil-low H16sc-ImP tumor model – which does not express the IL-1 ligands – failed to delay tumor growth, providing no therapeutic benefit (Supplementary Fig. S5J), despite the fact that *Il1rap* is expressed at higher levels in H16sc-ImP cancer cells compared with H16sc-ImP cancer cells (Supplementary Fig. S5K). Collectively, the data indicate that the observed growth delay in anti-IL1RAP–treated H16sc-IS1 tumors is in essence mediated by modulation of neutrophils.

Pharmacologic Inhibition of Pan–IL-1 Superfamily Signaling Reprograms the Immunosuppressive Neutrophils Underlying SIS

We next asked whether IL1RAP blockade was reprogramming neutrophils in addition to reducing their numbers in the periphery. To address this question, we performed bulk RNA-seq of neutrophils isolated from the BM, SP, and tumors of anti-IL1RAP–treated H16sc-IS1 tumor–bearing mice using IC-treated mice for comparison (Fig. 6A; Supplementary Table S2). Based on a Gene Ontology enrichment analysis (Fig. 6B), the cell cycle pathway was identified as downregulated in BM and splenic neutrophils upon anti-IL1RAP treatment, in line with the decreased myelopoiesis and neutrophil abundance observed in these compartments (Fig. 5D and E).

Interestingly, the antigen presentation pathway was conversely upregulated in anti-IL1RAP–treated peripheral neutrophils (Fig. 6B). Whereas the antigen-presenting capabilities of neutrophils in the TME have been well documented (43, 44), similar activity in peripheral sites remains largely unexplored. We therefore analyzed neutrophils in the BM, SP, and tumors after anti-IL1RAP therapy by flow cytometry and observed an increased proportion of neutrophils expressing costimulatory molecules, such as CD40 and CD86, alongside MHCI and MHCII molecules across all three compartments (Supplementary Fig. S6A–S6C). Interestingly, the proportion of neutrophils expressing $H2D^b$, the MHCI haplotype known to present the HPV16 E7 peptide used in the NP-E7LP vaccine (NP-E7LP Vax; refs. 9, 19), was elevated, suggesting that anti-IL1RAP–treated neutrophils might participate in eliciting adaptive immune responses to E7-based therapeutic vaccines.

Comparing splenic and intratumoral neutrophils, similar trends were observed upon anti-IL1RAP treatment. A signature of response to IL-1 was downregulated upon treatment in splenic and tumoral neutrophils (Fig. 6B). Moreover, several pathways related to neutrophil migration, inflammatory response, and protein secretion were downregulated. We also noted a reduction in reactive oxygen species (ROS) production in splenic neutrophils isolated from H16sc-IS1 tumor–bearing mice treated with anti-IL1RAP compared with IC (Fig. 6C). Given that ROS have been shown to suppress T-cell activity (3), these findings suggest that reductions in ROS may be a component of the immunostimulatory effects of anti-IL1RAP treatment. Additionally, expression of an "MDSC" mRNA signature was reduced in PANs and TANs (Fig. 6D). Collectively, these data indicate that anti-IL1RAP reprograms the immunosuppressive capacity of SIS-mediating neutrophils despite having only modest therapeutic efficacy as monotherapy.

Figure 3. IL-1 superfamily ligands induce SIS. **A,** Schematic representation of the time-course analysis. H16sc-IS1 tumor–bearing mice were sacrificed at different tumor volumes, and tumors, blood, and SPs were analyzed. **B,** Total myeloid cell ($CD11b^+$) and neutrophil expansion in the SP (right *y*-axis), and CD8 T cell suppression by splenic myeloid cells (left *y*-axis) during tumor progression. **C,** Correlation by simple linear regression between the SP size (SP/BW ratio) and cytokine concentration in the serum of H16sc-IS1 tumor–bearing mice. **D,** Quantification by flow cytometry of $CD11b^+$ total myeloid cells (left) and neutrophils (right) in the SP of H2b mice upon systematic administration of the indicated cytokines or PBS control. **E,** *In vitro* proliferation assay of anti-CD3/anti-CD28–activated CD8 T cells cocultured with $CD11b^+$ cells isolated from the SP of animals treated with the indicated cytokines. **F,** G-CSF concentration in the serum of H2b mice treated as indicated. For **D**–**F**: PBS ($n = 4$), IL-33 ($n = 4$), IL-36β ($n = 5$), IL-1α ($n = 5$), G-CSF ($n = 5$), and triplet-IL ($n = 4$). **G,** Growth curves of Ctrl H16sc-ImP ($n = 7$) and triplet-IL-OE H16sc-ImP (ILs-OE H16sc-ImP; $n = 6$) tumors. Spleen size (**H**), proportion of total myeloid cells ($CD11b^+$) and neutrophils in the BM and SP (**I**), and serum concentration of IL-1α, IL-36β, and G-CSF (**J**) of control (Ctrl) H16sc-ImP ($n = 7$) and ILs-OE H16sc-ImP ($n = 6$) mice. For **I,** Statistical significance computed with two-way ANOVA. **K,** Total myeloid cell ($CD11b^+$) and neutrophil expansion in the SP (right *y*-axis), and CD8 T-cell suppression by splenic myeloid cells (left *y*-axis) during progression of Ctrl H16sc-ImP vs. ILs-OE H16sc-ImP tumors. **L,** Proportions of immune cells in the SP compartment of Ctrl H16sc-ImP ($n = 7$), ILs-OE H16sc-ImP ($n = 6$), and H16sc-IS1 ($n = 6$) mice measured by flow cytometry. **M,** Quantification by flow cytometry of total myeloid cells ($CD11b^+$) and neutrophils in the TME of Ctrl H16sc-ImP ($n = 7$) and ILs-OE H16sc-ImP ($n = 6$) mice. **N,** Representative images (IF staining) of total myeloid cells ($CD11b^+$ in green), neutrophils ($Ly6G^+$ in red), and cancer cells ($K14^+$ in blue). Scale bar, 50 μm. The image is illustrative of the flow cytometry analysis shown in **M**. **O,** Proportions of immune cells in the tumor compartment of Ctrl H16sc-ImP ($n = 7$), ILs-OE H16sc-ImP ($n = 6$), and H16sc-IS1 ($n = 6$) mice measured by flow cytometry. Data in quantitative panels are presented as the mean ± SEM (*, $P < 0.05$; **, $P < 0.01$; ***, $P < 0.001$; ****, $P < 0.0001$; ns, no statistical significance; computed with the one-way ANOVA or Mann–Whitney, unless specified otherwise). ILs, IL-1 superfamily ligands; Treg, regulatory T cells.

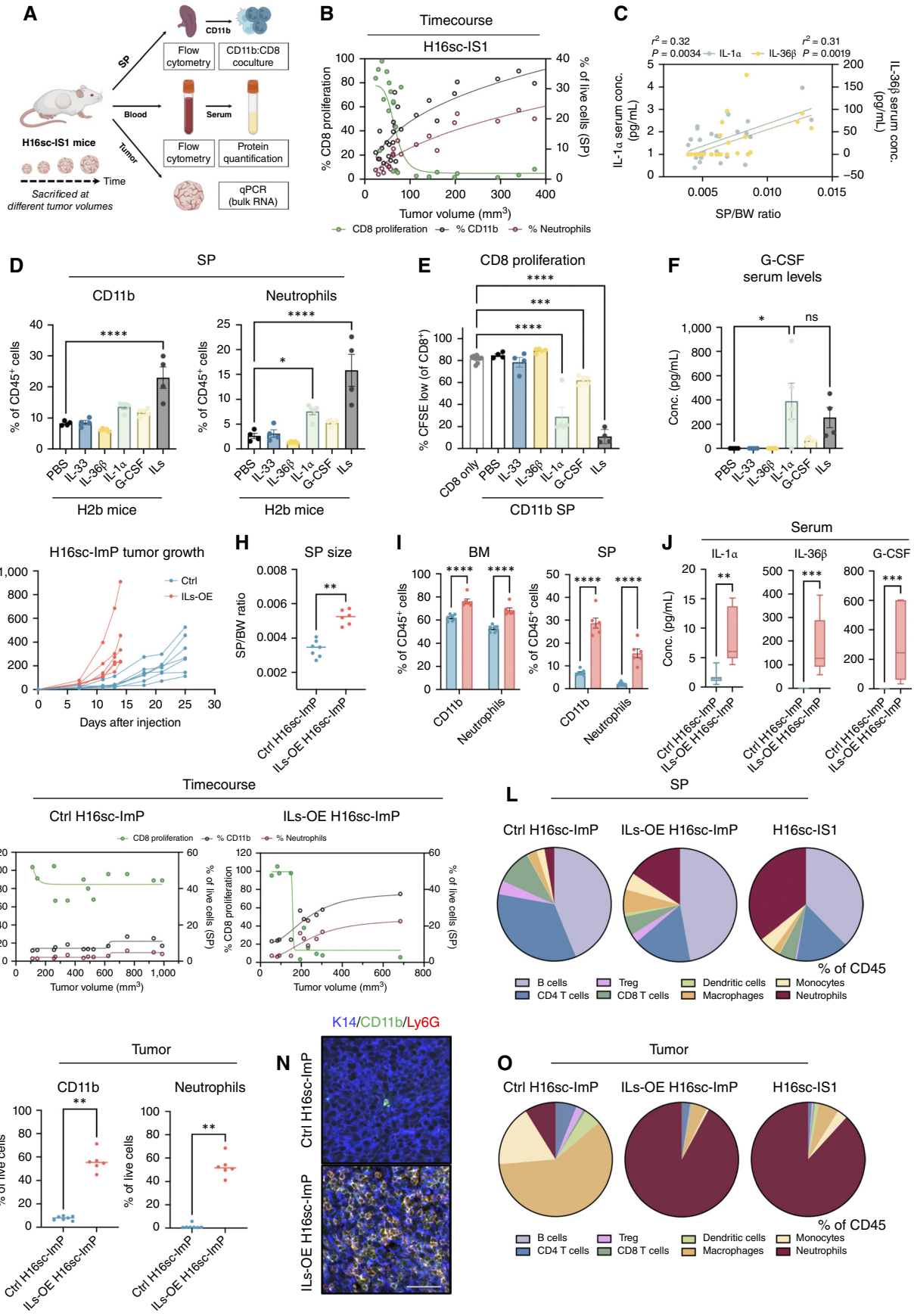

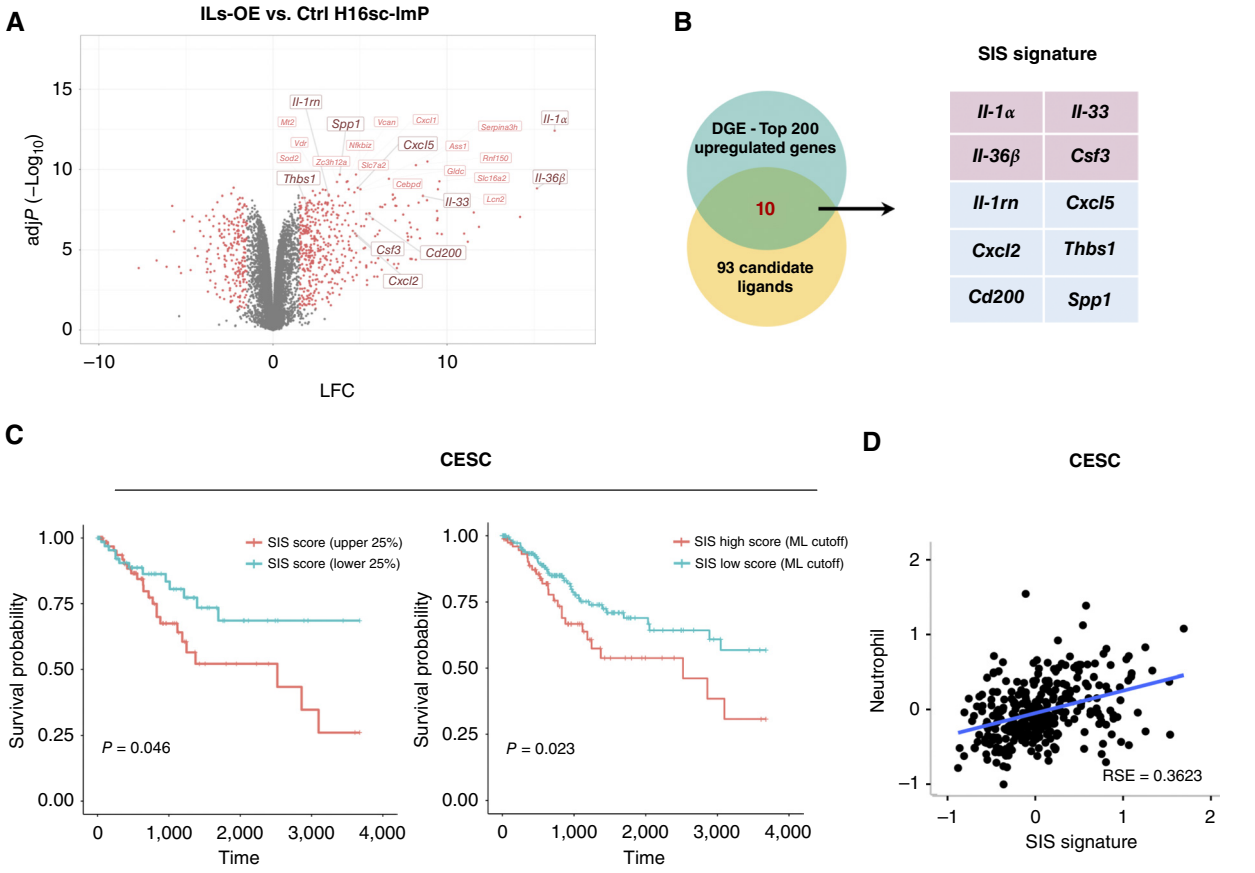

Figure 4. Assessing the IL-1 superfamily in human cervical cancer. **A,** Differentially expressed genes in triplet-IL-OE (ILs-OE H16sc-ImP) vs. control (Ctrl) H16-ImP cells, with adjusted *P* values (in $-\log_{10}$ scale) on the *y*-axis and $\log_2$ fold changes (LFC) on the *x*-axis. Genes with adjusted *P* values of <0.05 and $-1.5 > \text{LFC} > 1.5$ appear in red. Genes in dark red and bigger font-size are found in the SIS signature shown in B. **B,** Intersection between the top 200 genes induced in the ILs-OE H16sc-ImP tumors and the 93 candidate ligands from Fig. 2 (left), and the resultant 10-gene SIS signature (right). **C,** Survival analysis of patients with CESC (TCGA) defined according to their 10-gene SIS signature score. Left defined based on 25% lower (blue) and higher (red) SIS scores, and right defined based on machine learning cutoff for low (blue) and high (red) SIS scores. **D,** Correlation of the SIS signature score and estimated neutrophil abundance in patients with CESC (TCGA).

To functionally validate these observations, we performed an *ex vivo* coculture assay using activated CD8 T cells and splenic neutrophils isolated from H16sc-IS1 tumor–bearing mice, which confirmed the reduced immunosuppressive activity of peripheral neutrophils following anti-IL1RAP treatment (Fig. 6E). Additionally, we established a tumor antigen–specific coculture assay. CD8 T cells and total splenocytes from NP-E7LP–vaccinated mice were cocultured in the presence of the E7 peptide to restimulate E7-specific CD8 T cells, as measured by their ability to proliferate. Splenic neutrophils isolated from H16sc-IS1 tumor–bearing mice, treated or not with anti-IL1RAP, were added to this coculture to assess their capability to inhibit E7-specific CD8 T-cell proliferation (Fig. 6F). Remarkably, anti-IL1RAP treatment completely abrogated the immunosuppressive function of splenic neutrophils on antigen-specific CD8 T-cell responses (Fig. 6G). Notably, these data are particularly relevant to key steps in vaccine-induced immune responses, namely T-cell activation and expansion in the periphery. Furthermore, we investigated the impact of neutrophils on T-cell effector functions by performing a tumor-specific T cell–killing assay in the presence of neutrophils isolated from H16sc-IS1 tumor–bearing mice (Fig. 6H). Concordantly, we observed that anti-IL1RAP treatment almost completely reversed the immunosuppressive effect of neutrophils on T cell–mediated killing of cancer cells (Fig. 6I).

Anti-IL1RAP Improves Therapeutic Vaccine Response and Sensitizes Tumors to CTLA-4 Blockade

Given the capability of anti-IL1RAP monotherapy to interfere with the programming and expansion of immunosuppressive neutrophils, we combined anti-IL1RAP with NP-E7LP Vax, which is efficacious in the HPV16-expressing TC1 transplant model (8) but ineffective in the K14HPV16/H2b GEMM with SIS (9). The vaccine was administered 1 day after the first dose of anti-IL1RAP (Fig. 7A). Vaccination alone induced a modest response without tumor control, albeit better than anti-IL1RAP monotherapy. Notably, however, combining anti-IL1RAP with the vaccine led to a significantly improved response with sustained tumor control over an 18-day treatment period (Fig. 7B).

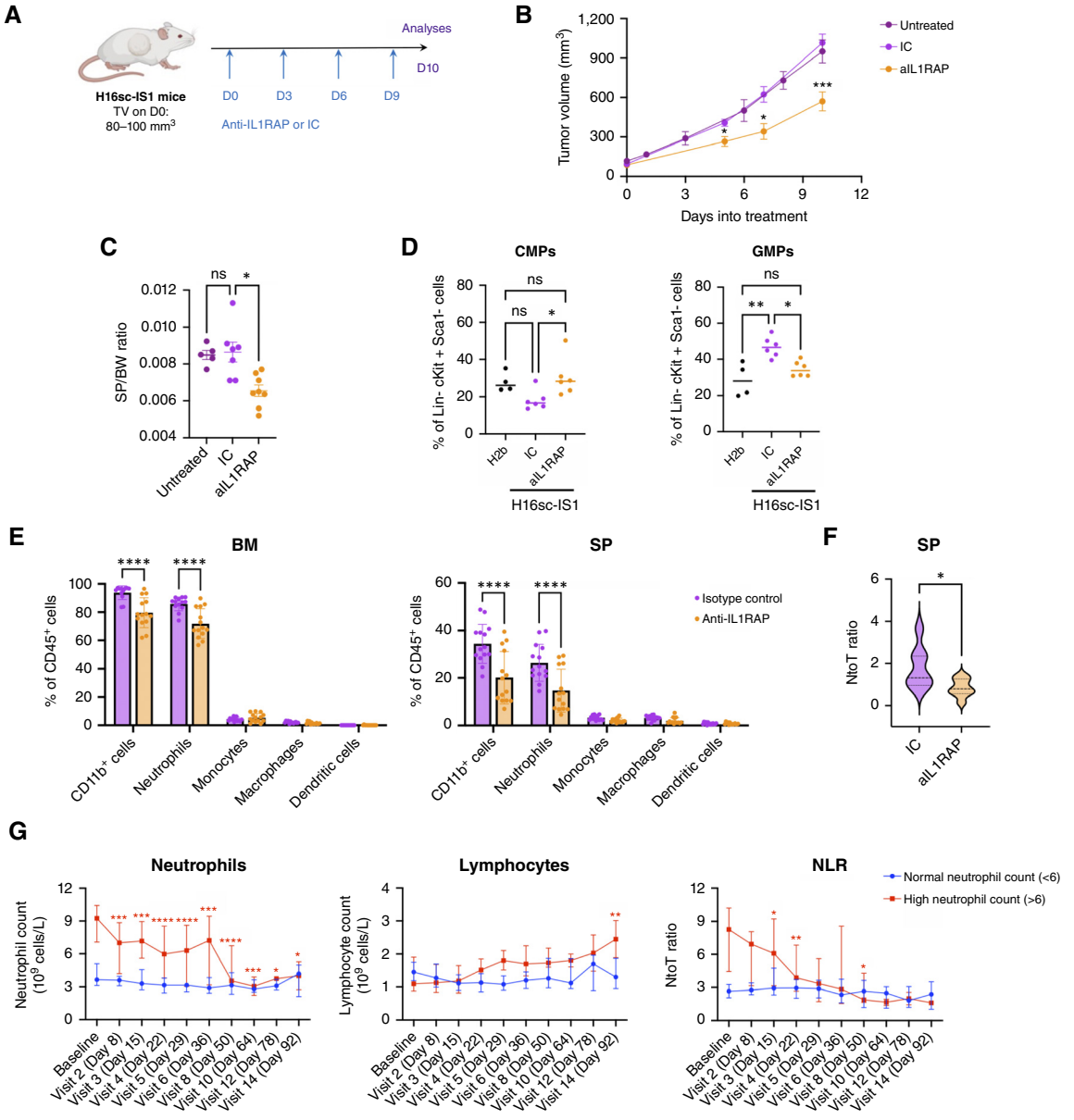

Figure 5. IL1RAP blockade disrupts systemic neutrophil expansion. **A,** Schematic representation of anti-IL1RAP (aIL1RAP) treatment regimen in H16sc-IS1 tumor–bearing mice. D, day; TV, tumor volume. **B,** Tumor growth curves in H16sc-IS1 tumor–bearing mice treated with aIL1RAP, IC or untreated control. Anti-IL1RAP (aIL1RAP)-treated and IC-treated groups were compared by the Mann–Whitney test at different timepoints. **C,** Spleen size of H16sc-IS1 tumor–bearing mice treated with aIL1RAP, IC, or untreated control. Statistical significance was computed with the Kruskal–Wallis test. **D,** Quantification by flow cytometry analysis on the BM of CMPs (Lin$^-$; c-Kit$^+$; Sca-1$^-$; FcγR$^-$; and CD34$^+$) and GMPs (Lin$^-$; c-Kit$^+$; Sca-1$^-$; FcγR$^+$; and CD34$^+$) from control H2b mice ($n = 4$) and H16sc-IS1 tumor–bearing mice treated with IC ($n = 6$) or aIL1RAP ($n = 6$). **E,** Quantification by flow cytometry analysis of different myeloid cell types [neutrophils (CD11b$^+$; Ly6G$^+$), monocytes (CD11b$^+$; Ly6G$^-$; Ly6C$^+$), macrophages (CD11b$^+$; Ly6G$^-$; Ly6C$^-$), and dendritic cells (CD11b$^+$; CD11c$^+$; MHCII$^+$) in the BM and SP of H16sc-IS1 tumor–bearing mice treated with aIL1RAP ($n = 14$) or IC ($n = 14$). Data are shown as the mean ± SD. **F,** The NtoT ratio measured by flow cytometry in SPs of H16sc-IS1 tumor–bearing mice treated with aIL1RAP ($n = 8$) or IC ($n = 8$). **G,** Neutrophil count, lymphocyte count, and their ratio (NLR) in the blood of patients with PDAC and NSCLC from the CANFOUR trial (NCT03267316) treated with aIL1RAP monotherapy (nadunolimab) on each visit (cycle of treatment). Patients were separated based on neutrophil count at baseline, with a cutoff of 6×10^9 cell/mL, resulting in a "normal neutrophil" group (baseline $< 6 \times 10^9$ cells/mL; $n = 20$) and a "high neutrophil" group (baseline $> 6 \times 10^9$ cells/mL; $n = 16$). Data are shown as the median + 95% confidence interval. To evaluate the effect of aIL1RAP treatment on blood cell count variation, a mixed effect statistical analysis, with Dunnett's multiple comparisons, was performed (all subsequent visits compared with baseline; *, $P < 0.05$; **, $P < 0.01$; ***, $P < 0.001$; ****, $P < 0.0001$; ns, no statistical significance; computed with one-way ANOVA, two-way ANOVA, or the Mann–Whitney test, unless specified otherwise).

To illuminate the basis for the therapeutic efficacy upon vaccination, we first focused on the periphery. We found that the combination of anti-IL1RAP plus NP-E7LP Vax decreased splenic myeloid cell numbers, especially neutrophils, by around 50% (Supplementary Fig. S7A). Furthermore, these myeloid cells were less suppressive when cocultured with CD8 T cells (Fig. 7C), which was associated with an increased abundance of effector CD8 T cells in the SP, especially tumor-specific ones

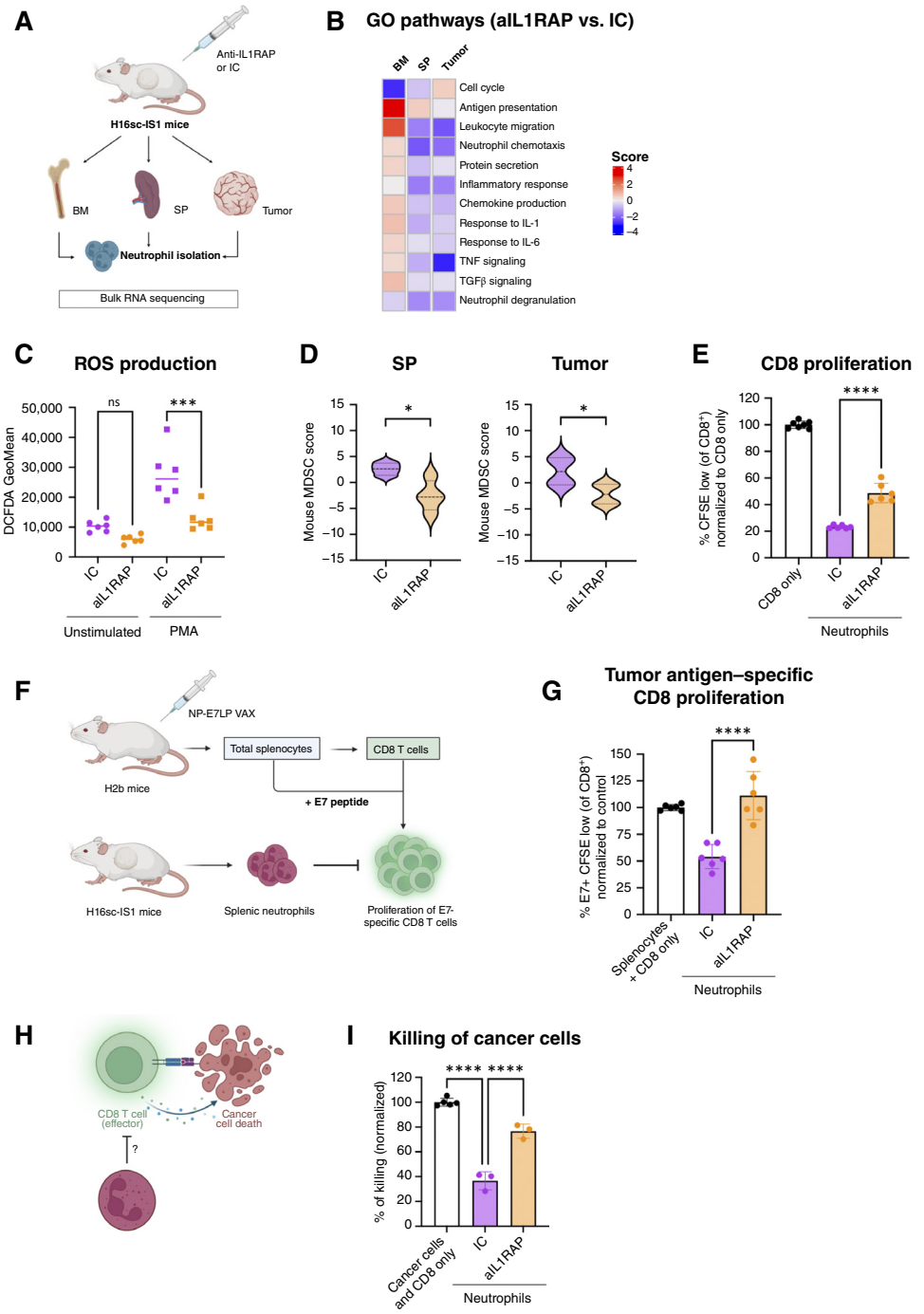

Figure 6. Blockade of IL1RAP reprograms immunosuppressive neutrophils. **A,** Schematic representation of the design for bulk RNA-seq analyses of neutrophils isolated from the BM, SPs, and tumors of H16sc-IS1 tumor–bearing mice treated for 7 days with anti-IL1RAP (aIL1RAP) or IC. **B,** Selected Gene Ontology pathways enriched in neutrophils isolated from the BM, SPs, and tumors of aIL1RAP- vs. IC-treated H16sc-IS1 tumor–bearing mice. Color scale reflects significance (= $\log_{10}$ of adjusted *P* value). Red and blue indicate induced and repressed pathways, respectively, computed by gene set enrichment analysis (GSEA). $N = 4$ per organ and per treatment. **C,** ROS production assay performed with neutrophils isolated from the SP of H16sc-IS1 tumor–bearing mice treated with aIL1RAP ($n = 6$) or IC ($n = 6$). **D,** MDSC gene signature score computed for neutrophils isolated from SPs and tumors in H16sc-IS1 tumor–bearing mice, treated either with IC ($n = 4$) or aIL1RAP ($n = 4$). **E,** *In vitro* proliferation assay of anti-CD3/anti-CD28–activated CD8 T cells alone or cocultured with neutrophils isolated from the SP of H16sc-IS1 tumor–bearing mice treated with IC ($n = 6$) or aIL1RAP ($n = 6$). **F,** Schematic representation of tumor antigen–specific proliferation assay of CD8 T cells cocultured with neutrophils. **G,** *In vitro* proliferation assay of E7-specific CD8 T cells restimulated with E7 peptide alone or cocultured with neutrophils isolated from the SPs of H16sc-IS1 tumor–bearing mice treated with IC ($n = 6$) or aIL1RAP ($n = 6$). **H,** Schematic representation of *in vitro* T cell–killing assay using H16sc-IS1 tumor-reactive CD8 T cells cocultured with H16sc-IS1 cancer cells alone or with neutrophils isolated from the SPs of H16sc-IS1 tumor–bearing mice treated with IC ($n = 3$) or aIL1RAP ($n = 3$). For **E**, **G**, and **I**, the data are shown as the mean ± SD (*, $P < 0.05$; **, $P < 0.01$; ***$P < 0.001$; ****, $P < 0.0001$; ns, no statistical significance; computed with one-way ANOVA, two-way ANOVA, or the Mann–Whitney test, unless specified otherwise).

(Supplementary Fig. S7A). There was also an increase in CD4 T cells, albeit with no change in the abundance of regulatory T cells (Supplementary Fig. S7A). Moreover, combining anti-IL1RAP plus NP-E7LP Vax led to a reduction in the peripheral neutrophil-to-T cell ratio (NtoT; Fig. 7D), which is similar to the NLR metric encompassing all lymphocytes.

Regarding effects on the TME, in line with the previous figure, anti-IL1RAP plus NP-E7LP Vax did not discernably alter the intratumoral myeloid compartment compared with vaccination alone (Supplementary Fig. S7B). However, we observed a substantial CD8 influx, notably tumor-specific, cytotoxic, and proliferative CD8 T cells (Fig. 7E), which was not observed in the context of anti-IL1RAP monotherapy (Supplementary Fig. S5F). Interestingly, we also observed an increased abundance of central memory CD8 T cells in mice that had received the double combination therapy (Fig. 7E). To confirm the pivotal role of CD8 T cells in mediating tumor control, we performed a CD8 depletion experiment, which completely abrogated the survival benefit observed in treated mice (Fig. 7F). Moreover, the otherwise high tumoral NtoT ratio (Fig. 7G) was reduced, which is associated with a lower survival probability in patients with CESC (Supplementary Fig. S7C).

We next addressed a salient question about the relevance of simultaneously targeting with anti-IL1RAP the parallel signaling pathways induced by the three IL molecules, as contrasted to only blocking the IL-1α/β pathway, which is known for its role in SIS induction in other tumor types (10, 45). To investigate this question, we vaccinated H16sc-IS1 tumor–bearing mice in combination with either anti–IL-1β, anti–IL-1R, or anti-IL1RAP. We observed that targeting the IL-1 α/β pathway alone (thus keeping IL-33– and IL-36β–induced pathways active) was insufficient to achieve the full benefits of IL1RAP blockade. Vaccination combined with anti–IL-1β did not improve survival, and anti–IL-1R showed only modest effects (Fig. 7H). These findings support the rationale for simultaneously targeting the three IL molecules to control SIS and enable vaccine responses.

Aiming to improve upon the therapeutic benefit of the dual combination, we assessed an obvious candidate, G-CSF/CSF3. Surprisingly, the incorporation of a neutralizing antibody against G-CSF did not produce any additive benefit. Rather, the addition of anti–G-CSF on top of anti-IL1RAP plus NP-E7LP Vax elicited, after 12 days of treatment, a loss of tumor control (Supplementary Fig. S7D) that was associated with increased SP size (Supplementary Fig. S7E), and enhanced neutrophil infiltration and decreased abundance of CD8 and CD4 T cells in the TME (Supplementary Fig. S7F).

Given this unexpected interference upon cotargeting neutrophils, we instead considered the possibility of boosting the T-cell priming step of the therapeutic vaccine response. To do so, we combined our dual regimen with an anti–CTLA-4 mAb, which is known to disrupt a major barrier to T-cell priming and is reported to synergize with various cancer vaccination regimens (46–48). The addition of anti–CTLA-4 considerably increased the survival benefit, from a median survival of 38 days for the doublet to 59 days for the triplet combination (Fig. 7I). It is notable that, at the defined endpoint of the study, 20% of the animals remained disease-free. The therapeutic benefit of anti–CTLA-4 for an efficacious vaccine response required the SIS-inhibiting anti-IL1RAP antibody, as the dual combination of anti–CTLA-4 plus the vaccine lacking it had minimal efficacy (Fig. 7I). Given this lack of response, we did not test anti–CTLA-4 by itself.

As anticipated, given that it directly targets T cells, the inclusion of anti-CTLA-4 in the triple combination was not associated with changes in the neutrophil compartments in the SP or tumor (Supplementary Fig. S7G) but rather with a modulation of the lymphoid compartment in tumors, in which the proportions of CD4 and CD8 were appreciably increased (Fig. 7J; Supplementary Fig. S7G). The most striking effects were on CD8 T cells: the abundances of tumor-infiltrating effector, cytotoxic, and proliferative CD8 T cells in the triple therapy were increased compared with the double combinations lacking either anti–CTLA-4 or anti-IL1RAP (Fig. 7J). We confirmed these results in triplet-IL-OE H16sc-ImP tumors, in which, as expected, the overexpression of SIS-inducing factors blocked the vaccine response, producing no survival benefit (Supplementary Fig. S7H). In marked contrast, addition of anti-IL1RAP rescued the vaccine response, which was further improved by combining it with anti–CTLA-4 (Supplementary Fig. S7H).

DISCUSSION

An important agenda for cancer research has been to illuminate the constitution of the TME, wherein functional capabilities – hallmarks of cancer – acquired during tumorigenesis and malignant progression manifest cancer as a life-threating disease (1, 49). One facet involves the recruitment of tumor-promoting myeloid cells that emigrate to populate the TME, fostering diverse tumor phenotypes, including angiogenesis, invasion and metastasis, and immune evasion (3–5, 50–52). Looking beyond the TME, however, it is increasingly appreciated that cancer is also a systemic disease (7, 53, 54). In particular, there is increasing evidence for SIS, whereby the induction of antitumoral adaptive immune responses is abrogated in the BM and peripheral lymphoid organs, complementing the immune barrier constituted in the TME (7, 11). Having previously described a state of SIS associated with an expansion of immunosuppressive neutrophils in SP and lymph nodes in a mouse model of HPV16-induced cervical cancer (9), we have now deeply characterized this phenotype and identified its mechanistic basis: squamous cancer cells expressing the HPV16 oncogenes secrete IL-1 ligands – IL-1α, IL-33, and IL-36β – into the circulatory system, whereby they program differentiation in the BM and expansion of distinctive neutrophil subtypes, in particular immunosuppressive ones, that populate the SP and tumor. The aberrant neutrophil expansion is dependent on this triplet of IL-1 ligands, as evidenced by the collective inhibition of their distinctive receptors via antibody-mediated blockade of a common subunit, IL1RAP. Inhibition of pan–IL-1 signaling reprograms neutrophil development, which disrupts SIS, rendering an otherwise immunoevasive tumor type responsive to immunotherapy.

Human cervical cancer induced by high risk HPVs is the second most common cause of cancer-related death worldwide in women aged 15 to 44 years (55) and fourth overall (56).

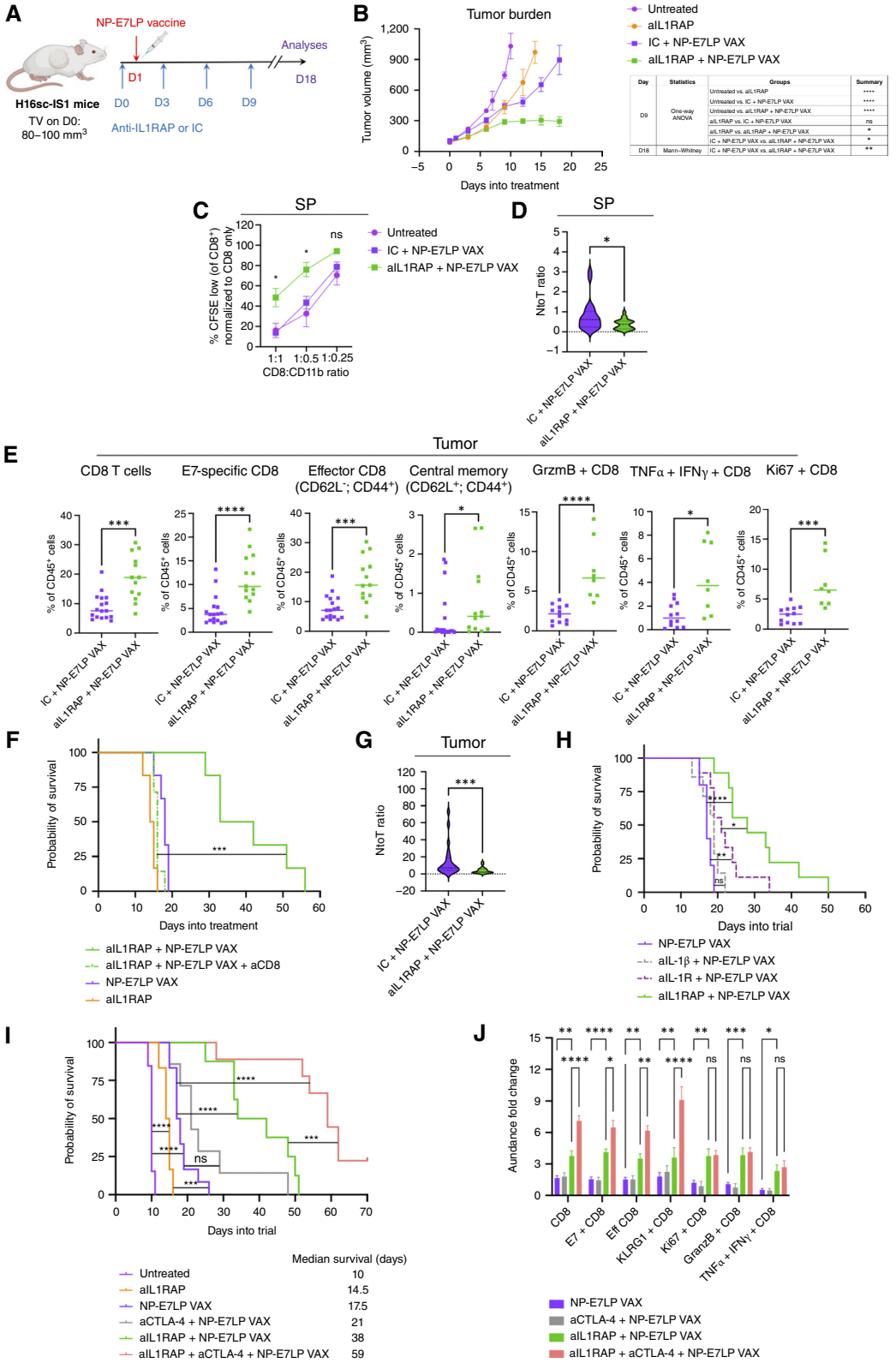

Figure 7. Anti-IL1RAP (aIL1RAP) therapy improves vaccine response and cooperates with anti-CTLA-4 blockade. **A,** Schematic representation of the aIL1RAP plus vaccine (VAX) treatment regimen in H16sc-IS1 tumor–bearing mice. D, day; TV, tumor volume. **B,** Tumor growth curves of treated H16sc-IS1 tumors. Untreated ($n = 18$), aIL1RAP ($n = 13$), IC + NP-E7LP VAX ($n = 17$), aIL1RAP + NP-E7LP VAX ($n = 13$). Statistical significance computed with one-way ANOVA and the Mann–Whitney test as specified. **C,** *In vitro* proliferation assay of anti-CD3/anti-CD28–activated CD8 T cells cocultured (at 1:1, 1:0.5, and 1:0.25 ratios) with splenic CD11b cells isolated on day 18 (treated mice) or at a necessarily earlier endpoint of day 10 (*continued on following page*)

In contrast to the success of prophylactic vaccines, HPV16-based oncoprotein vaccines have minimal efficacy against invasive cervical carcinomas (57–59), much like in our GEMM (9). Moreover, conventional and targeted therapies have limited efficacy (60–62). As such, an important agenda is to develop effective therapies for HPV-driven cervical cancers. The work presented herein suggest a path forward for vaccines and other immunotherapies in human cervical cancer, involving the disruption of SIS (and inferentially the immunosuppressive TME) induced by a triplet of IL-1 ligands via blockade of IL-1 superfamily receptor signaling, which unlocks therapeutic efficacy of a prototypical HPV16 vaccine. To assess the possible association of SIS induced by IL-1α/β, IL-33, and IL-36β in human cervical cancer, we developed a 10-gene signature that predicts poorer survival in a TCGA cohort of CESC. Interestingly, our SIS signature includes two chemokines, CXCL2/5, which are known to stimulate neutrophil recruitment, whose therapeutic blockade has shown benefit in preclinical trials, reducing neutrophil abundance concomitant with enhancing tumor-antagonizing T-cell responses in mouse models of pancreas and other cancers (25, 63, 64). Our data suggest that CXCL2/5 are upregulated by IL-1 superfamily signaling as a component of the SIS program they induce.

Beyond HPV16-driven cervical cancer, our SIS signature and other bioinformatic analyses of a TCGA tumor dataset have implicated SIS in significant subsets of the head and neck (HNSC), lung (LUSC), and invasive bladder cancer (BLCA), along with rare subsets of other tumor types. We suspect that subsets of additional human cancers beyond the 13 analyzed herein may also present with this form of multi-IL-1–induced SIS, which could be identified with our gene signature. Concordantly, the importance of IL-1 signaling in cancer is being increasingly recognized, principally involving IL-1β, which shares its receptor with IL-1α. Thus, a clinical trial of an anti-IL-1β mAb (canakinumab) for treating symptoms of atherosclerosis unexpectedly revealed a reduced incidence of lung cancer (65). In contrast, however, to this "prevention trial", subsequent phase III intervention trials (CANOPY-A, -1, and -2) in NSCLC failed to meet their endpoints (66–68), suggesting functional redundancy or insufficiency in established tumors for IL-1β–induced signaling. Nevertheless, a series of studies in mouse models of breast cancer, in which IL-1β and/or IL-1α was similarly inhibited, have established roles for IL-1 signaling in the TME and for SIS (10, 45, 69). Parenthetically, it will be interesting to assess tumors relapsing on therapies singularly targeting anti–IL-1β, as our study suggests that a logical adaptive resistance mechanism might involve upregulation of IL-1α, IL-33, and/or IL-36β, which could then be targeted with anti-IL1RAP and other pan–IL-1 inhibitors (66–68). These broader considerations notwithstanding, our focus has been on elucidating and abrogating SIS in HPV16-induced cervical cancer, giving the important opportunity to unlock the suppressed potential of oncoprotein vaccines in the context of a combinatorial immunotherapy, as discussed below.

The data presented herein indicate that IL-1α, IL-33, and IL-36β have overlapping but only partially redundant functional roles in stimulating expression of genes involved in SIS, as revealed by comparative analysis and genetic perturbation of cancer cell lines with distinctive SIS phenotypes derived from our mouse model of cancer-induced SIS, and by evaluating their individual and collective effects in a cell-based model of myeloid differentiation into neutrophils. Moreover, inoculation of normal mice with the three IL-1 ligands induces a similar expansion of immunosuppressive neutrophils in BM and SP. A prominent candidate for regulation of SIS, G-CSF/CSF3, which stimulates expansion of neutrophils, cannot recapitulate these effects but rather is evidently induced by and then collaborates with IL-1 superfamily signaling to elicit SIS *in vivo* and to inhibit CD8 T-cell proliferation in coculture bioassays.

The overlapping and complementary roles of IL-1α, IL-33, and IL-36β in stimulating immunosuppressive myeloid expansion, and the demonstrable capability to inhibit this effect by targeting the common subunit – IL1RAP – of their distinctive heterodimeric receptors, motivated therapeutic trials that revealed the importance of SIS for expansive tumor growth. As monotherapy, anti-IL1RAP decreased SP size, lowered the abundance of neutrophils in the SP, and consequently reduced the NtoT ratio therein. Moreover, anti-IL1RAP also downregulated the aforementioned immunosuppressive "MDSC" gene signature in the SP and tumors and rescued antigen-specific T-cell proliferation when cocultured with peripheral neutrophils. Thus, blockage of IL-1 superfamily signaling reprogrammed neutrophil expansion and phenotype, significantly attenuating SIS, concomitant with a modest impairment in tumor growth. Although all experiments point toward a prominent role for neutrophils in the antitumor mechanism of anti-IL1RAP, we cannot fully exclude the possibility that anti-IL1RAP may modulate other less abundant cell types expressing IL1RAP. Notably, these preclinical trials and those discussed below were performed

Figure 7. ***(Continued)*** (untreated mice). Untreated ($n = 3$), IC + NP-E7LP VAX ($n = 10$), aIL1RAP + NP-E7LP VAX ($n = 14$). **D,** The NtoT ratio, measured by flow cytometry, in the SPs of treated H16sc-IS1 mice on day 18. **E,** Proportion of different CD8 T-cell types in tumors of H16sc-IS1 mice on day 18, treated as indicated, measured by flow cytometry. For **D** and **E**: IC + NP-E7LP VAX ($n = 17$), aIL1RAP + NP-E7LP VAX ($n = 13$). **F,** Survival trial assessing the importance of CD8 T-cell responses in the aIL1RAP plus NP-E7LP VAX combinatorial treatment by using an anti-CD8 antibody depletion strategy. Several regimens were compared: aIL1RAP alone ($n = 6$), NP-E7LP VAX alone ($n = 6$), or NP-E7LP VAX plus aIL1RAP combined or not with anti-CD8 treatment, ($n = 7$) and ($n = 6$), respectively. **G,** The NtoT ratio, measured by flow cytometry, in the tumors of treated H16sc-IS1 mice on day 18. IC + NP-E7LP VAX ($n = 13$), aIL1RAP + NP-E7LP VAX ($n = 16$). **H,** Survival trial assessing the relevance of cotargeting the parallel signaling pathways induced by the multiple IL molecules compared with blocking the IL-1α/β pathway alone. NP-E7LP VAX-treated mice ($n = 10$) were compared with mice treated with NP-E7LP VAX combined either with aIL1RAP ($n = 9$), anti-IL-1R (aIL-1R; $n = 9$), or anti-IL-1β (aIL-1β; $n = 7$). **I,** Survival trial assessing the effect of combinatorial regimens involving NP-E7LP VAX with aIL1RAP and/or anti-CTLA-4 (aCTLA-4), in H16sc-IS1 tumor–bearing mice. Untreated ($n = 13$), aIL1RAP ($n = 6$), NP-E7LP VAX ($n = 12$), aCTLA-4 + NP-E7LP VAX ($n = 7$), aIL1RAP + NP-E7LP VAX ($n = 8$), and aIL1RAP + aCTLA-4 + NP-E7LP VAX ($n = 9$). For **F**, **H**, and **I**, statistical significance was computed with Mantel–Cox tests. **J,** Flow cytometry analysis on day 18 of CD8 T-cell subtypes in the tumor, normalized to the untreated condition. Untreated ($n = 7$), NP-E7LP VAX ($n = 11$–17), aCTLA-4 + NP-E7LP VAX ($n = 3$), aIL1RAP + NP-E7LP VAX ($n = 9$–13), and aIL1RAP + aCTLA-4 + NP-E7LP VAX ($n = 6$). Data in quantitative panels are presented as the mean ± SEM (*, $P < 0.05$; **, $P < 0.01$; ***, $P < 0.001$; ****, $P < 0.0001$; ns, no statistical significance; computed with two-way ANOVA or the Mann–Whitney test, unless specified otherwise).

in mice bearing tumors from the SIS-inducing H16sc-IS1 cancer cell line that was derived from a skin tumor in the K14HPV16/H2b GEMM. Unfortunately, strict veterinary policies in Switzerland have precluded preclinical trials on mice bearing *de novo* cervical and skin tumors in the GEMM.

Given that we had previously implicated SIS in the lack of efficacy of a potent peptide vaccine based on the E7 oncoprotein of HPV16 (8, 9), we assessed the potential of anti-IL1RAP to enable its therapeutic activity by attenuating SIS. Indeed, the combination showed improved efficacy and survival benefit compared with either monotherapy. We also established the relevance of cotargeting IL-1α, IL-1β, IL-33, and IL-36β using anti-IL1RAP, as opposed to selectively interfering with the IL-1 pathway, given that anti–IL-1β or anti–IL-1R combined with NP-E7LP Vax showed no or a modest response, respectively. These results are indicative of complementary roles for the IL-1 ligands in inducing this form of SIS. Seeking to further improve upon the benefits of anti-IL1RAP, and reasoning that other tumor-derived factors could be contributing to the expansion of immunosuppressive neutrophils, we incorporated anti–G-CSF/CSF3 in a triple therapy. Surprisingly, the inclusion of anti–G-CSF/CSF3 counteracted the benefits of anti-IL1RAP after 14 days of treatment, increasing neutrophil and decreasing CD8 T-cell abundance in the TME and restoring tumor growth. Noting that G-CSF is a downstream effector of IL-1 signaling that helps induce and exacerbate SIS, these data seem counterintuitive. However, a few points warrant consideration. First, it seems that cancer cells have the ability to upregulate G-CSF/CSF3 in an IL-1–independent manner, as shown by the unchanged *Csf3* mRNA expression upon *Il1rap* knockdown in cancer cells. Additionally, it is unclear whether anti–G-CSF is neutralizing all bioavailable G-CSF, such that relapsing tumors could either increase G-CSF production or bypass its activity by producing an alternative growth factor such as GM-CSF. Concordantly, we previously reported that anti–G-CSF had no benefit combined with NP-E7LP Vax (in the absence of IL-1 blockade; ref. 9). We now suspect that inhibiting G-CSF, an essential neutrophil growth factor, in addition to pan-IL-1 signaling, exerts strong selective pressure on the granulocytic compartment, eliciting an early adaptive resistance that results in alternative mechanisms of SIS, characterized by a rebound in neutrophil numbers and associated loss of tumor control upon vaccination. Focusing instead on the T-cell compartment, considering that the CTLA-4 checkpoint is known to limit vaccine-induced T-cell priming and the activation of *de novo* immune responses (46), we incorporated anti–CTLA-4 into the regimen. This triple combination proved beneficial, impairing tumor growth and increasing survival, concomitant with markedly increasing the abundance and activity of tumor-infiltrating T cells. Thus, whereas the HPV16 E7 vaccine had minimal efficacy as monotherapy, the mechanism-guided combination of targeting neutrophils with anti-IL1RAP and T-cell priming with anti–CTLA-4 produced significant therapeutic benefit.

In conclusion, by elucidating a mechanism of SIS induced by pan–IL-1 signaling, and demonstrating a therapeutic strategy to disrupt it, our results encourage consideration of clinical trials in patients with cervical carcinomas, combining anti-IL1RAP or other pan–IL-1 superfamily inhibitors with HPV oncoprotein–derived vaccines and anti–CTLA-4, and conceivably other immunomodulatory agents, constituting a next-generation immunotherapy with potentially ground-breaking efficacy. Finally, investigating alternative therapeutic combinations that do not include the vaccine, such as anti-IL1RAP plus other immune checkpoint inhibitors, is a topic worthy of future investigation.

METHODS

Mouse Models

For all experiments, K14HPV16/H2b mice (European Mouse Mutant Archive ID EM:15289) or their FVBN/H2b littermates (EM:15300) were used. A characterization of the K14HPV16/H2b model was reported previously (8, 9). The K14HPV16/H2b line was generated by crossing K14HPV16/FVBN (H2q) mice (13, 14) with C57BL/6 (H2b) mice to introduce the entire H2b locus, followed by backcrossing to FVBN to render the mice congenic for H2b but otherwise genetically FVBN. This genetic configuration allows K14HPV16/H2b mice to present E7-derived peptides on MHCI molecules while maintaining the FVBN background that is permissive for squamous carcinogenesis. F1 mice were backcrossed for 11 generations to FVBN, selecting for the H2b locus in every generation by flow cytometry analyses of H2Kb and H2Db. Afterward, nontransgenic mice were intercrossed to generate homozygous FVBN/H2b congenic mice expressing H2Kb and H2Db but not H2Kq and H2D/Lq. To maintain the GEMM, K14HPV16/H2b males were crossed to FVBN/H2b females, and transgenic progeny were identified by PCR of toe biopsies (forward primer: ACCCAGAAAGT TACCACAGTTATGC; reverse primer: TGCTTGCAGTACACACATT CTAAT) using the Transnetyx Genotyping service (https://quickorder.transnetyx.com/). K14HPV16/H2b females were subcutaneously implanted with estrogen-releasing pellets at ages 1, 3, and 5 months to obtain cervical tumors.

The H16sc-IS1, H16sc-Int and H16sc-ImP cancer cell lines were derived by authors from skin SCCs arising in K14HPV16/H2b mice. Cancer cell lines were cultured in RPMI (Thermo Fisher Scientific), 10% FBS (Thermo Fisher Scientific), and penicillin/streptomycin (100 U/mL penicillin and 100 μg/mL streptomycin; Thermo Fisher Scientific). All cell lines were routinely tested for *Mycoplasma*.

For syngeneic tumor models, 0.7×10^6 (H16sc-IS1) or 1.0×10^6 (H16sc-Int and H16sc-ImP) cancer cells were implanted subcutaneously in 100 μl PBS/Matrigel (Corning, 1:1 solution) into the flank of 6- to 9-week-old FVBN/H2b mice. Tumor growth was measured with a caliper using the formula $V = W^2L\pi/6$. All experiments were performed in accordance with Swiss law and with the ethical approval of the Cantonal Veterinary Office of Canton de Vaud, Switzerland. The design of the experimental trials and follow-up analyses are presented in the Results section. For detailed information on sample size and statistical methods, please see the presented figures or associated figure legends.

CFU Cultures of Mouse HSPCs

For CFU assays, HSPCs were enriched from BM single-cell suspensions of K14HPV16/H2b and FVBN/H2b mice using EasySep Mouse Hematopoietic Progenitor Cell Isolation Kit (Stemcell Technologies) according to the manufacturer's instructions. Isolated HSPCs were resuspended at a cell density of 0.2×10^6 cells/mL in complete media: IMDM + 2% FBS + 1% penicillin/streptomycin (Thermo Fisher Scientific). A measure of 10^5 cells were plated in each well of an ultra-low attachment 24-well plate (500 μL/well), and another 500 μL of complete culture media, supplemented or not with 20% mouse serum, were added on top. Mouse serum was used at a final concentration of 10%. HSPCs were incubated overnight at 37°C, 5% CO_2. The next day, cells were harvested, counted,

and resuspended at 10^4 cells/mL in complete media. A measure of 400 µL of cells were added to 4 mL of prealiquoted methylcellulose-based MethoCult media optimized for the growth of granulocyte–macrophage progenitor cells. HSPC-containing MethoCult media was then vortexed and allowed to stand at room temperature for 5 minutes, and 1.1 mL were plated in triplicate in a six-well plate. Plates were incubated in a moist chamber at 37°C, 5% CO_2, for 8 days. On day 8, individual colonies were counted under a microscope and characterized based on their morphologic features. Three distinct types of colonies could be observed: CFU-GM, CFU-G, and CFU-M. Whereas CFU-GM arises from bipotent progenitors, GFU-G and CFU-M arise from unipotent progenitors and give rise to cells of granulocytic and monocytic lineages, respectively. Data were plotted in GraphPad Prism (RRID: SCR_002798) v9 according to the treatment groups.

Differentiation of HoxB8 Progenitors

HoxB8 neutrophil progenitors and stem cell factor (SCF)-producing Chinese hamster ovary (CHO) cells were kindly gifted by Prof. Thomas Kaufmann (University of Bern, Switzerland). HoxB8 progenitors were cultured in RPMI (Thermo Fisher Scientific), 10% FBS (Thermo Fisher Scientific), 1% penicillin/streptomycin (Thermo Fisher Scientific), 50 µmol/L 2-Mercaptoethanol (Thermo Fisher Scientific), and 10% conditioned media from SCF-producing CHO cells. HoxB8 cells were kept in the immortalized progenitor state by addition of 0.1 µmol/L 4-hydroxytamoxifen (4-OHT) to the culture media. To initiate neutrophil differentiation, cells were washed 3× with PBS to remove all traces of 4-OHT. Cells were then resuspended at 2.5×10^4 cells/mL in complete media (without 4-OHT) supplemented or not with recombinant cytokines. Recombinant mouse IL-1α, IL-33, and G-CSF were purchased from Peprotech and used at a concentration of 0.5 ng/mL. Recombinant mouse IL-36β was purchased from R&D Systems and used at a concentration of 0.5 ng/mL. Cells were plated in six-well plates (3 mL/well) and incubated at 37°C, 5% CO_2, for 5 days. Differentiation media were replenished on day 3. On day 5, differentiated HoxB8 neutrophils were collected by centrifugation and used for further analysis.

Systemic Administration of Recombinant Cytokines

Recombinant mouse G-CSF, IL-1α, and IL-33 were purchased from Peprotech. Recombinant mouse IL-36β was purchased from R&D Systems. Cytokines were systemically administered into 6- to 9-week-old FVBN/H2b mice by repeated intraperitoneal injection. Mice were injected on days 0, 2, 5, and 7 (for a total of 4 injections/mouse) and were sacrificed on day 8. IL-1α and G-CSF were administered at 0.25 µg/dose. IL-33 and IL-36β were administered at 0.5 µg/dose.

Therapeutic Trials

Mouse-specific antibodies molecules were administered intraperitoneally, as described below, once the tumors reached the tumor volume defined in the experimental setup (Results section) using simple randomization. Anti-IL1RAP (mNadunolimab, clone 3A9, property of Cantargia AB) and matched IC (mouse IgG2a), both provided by Cantargia AB, were injected at 500 µg/mouse for the first dose, followed by 250 µg/mouse every 3 days. Anti–CTLA-4 (Bio X Cell, clone 9D9) was injected at 250 µg/mouse every 3 days. Anti–G-CSF (Thermo Fisher Scientific, Cat# 16-7353-38, RRID: AB_2866300) was injected at 100 µg/mouse 3 times a week. NP-E7LP Vax was administered as a single dose 1 day after antibody treatment start.

NP-E7LP Vaccine Preparation and Immunization

The CpG-B 1826 oligonucleotide (5′-TCCATGAGCTTCCTG ACGTT-3′ as phosphorothioated DNA bases) was purchased from Microsynth and used as adjuvant in vaccine formulations. HPV16 E7 long peptide (aa 43–77: GQAEPDRAHYNIVTFCCKCD-STLRLCVQSTHVDIR, purity >90%) was purchased from Think Peptides and used for nanoparticle (NP) conjugation. NPs were synthesized, functionalized, and characterized as previously described (70–72). For antigen conjugation, the HPV16 E7 long peptide was dissolved in DMSO and incubated for 12 hours in endotoxin-free water at room temperature in the presence of NPs and guanidine hydrochloride (AppliChem) at room temperature. NP-E7LP was purified by size-exclusion chromatography using CL-6B matrix (Sigma-Aldrich), eluted, and stored in PBS at room temperature. E7LP loading on the NPs was measured by bicinchoninic acid assay (Thermo Fisher Scientific). NPs alone have been shown to have no adjuvant activity. Mice were immunized with a total amount 15 µg of E7LP in the NP-bound form, and 40 µg of CpG was used as adjuvant. Nonimmunized mice were treated with PBS. Mice received 1 shot of vaccine as indicated in the text. Subcutaneous immunizations of mice were performed in the four limbs using the Hock method (73).

Preparation of Cell Suspensions

BM single-cell suspensions were generated from femurs and tibiae of mice. Cells were flushed by centrifuging the bones cut at the knee joint. The isolate was filtered through a 40 µm cell strainer. Single-cell suspensions of SPs were generated by mashing the SP through a 40 µm cell strainer. Tumors were harvested and minced using a scalpel and digested for 30 minutes using collagenase A (0.33 U/mL, Roche), dispase (0.85 U/mL, Roche), and DNAse I (144 U/mL, Roche) in RPMI medium with intermittent shaking at 37°C. Afterward, tumor single-cell suspensions were passed through a 70 µm cell strainer. Blood was collected by intracardiac puncture into EDTA-coated tubes. Red blood cells were lysed with BD Pharm Lyse Lysing buffer (BD Biosciences, ref. 555899) according to the manufacturer's instructions. Cell suspensions were further used for flow cytometry analysis, cell isolation, or scRNA-seq.

Proliferation of Anti-CD3/Anti-CD28–Activated CD8 T Cells Cocultured with Total Myeloid Cells or Purified Neutrophils

CD8 T cells were magnetically isolated from the SP using Easysep Mouse $CD8^+$ T cell Isolation Kit (Stemcell Technologies) according to the manufacturer's instructions. Total CD11b cells were magnetically isolated from the SP and tumor using EasySep Mouse CD11b Positive Selection Kit II (Stemcell Technologies) according to the manufacturer's instructions. Neutrophils were magnetically isolated from the SP using the mouse Anti-Ly-6G MicroBeads UltraPure Kit (Miltenyi Biotec) according to the manufacturer's instructions. For proliferation assays, CD8 T cells were labelled with CFSE and cocultured with total CD11b cells or neutrophils in a 1:1 ratio (unless specified otherwise) with anti-CD3/anti-CD28 Dynabeads for T-cell activation and expansion. Cocultured cells were harvested 48 to 72 hours later, stained with a viability dye (LIVE/DEAD Fixable Violet Dead Cell Stain Kit, Invitrogen), and analyzed by flow cytometry to assess their proliferation.

Tumor Antigen–Specific Proliferation of CD8 T Cells Cocultured with Neutrophils

Single-cell suspensions of SPs (total splenocytes) and splenic CD8 T cells from NP-E7LP–vaccinated mice were obtained as previously described. Neutrophils were isolated from the SP as previously described. For tumor antigen–specific proliferation assays, CD8 T cells were labelled with CFSE and restimulated with 1 µg/mL of the HPV16 E7 peptide RAHYNIVTF in the presence of total splenocytes and neutrophils at a 1:1:1 ratio. Cocultured cells were

harvested 72 hours later, stained with a viability dye (LIVE/DEAD Fixable Violet Dead Cell Stain Kit, Invitrogen), and analyzed by flow cytometry to assess their proliferation.

ROS Production Assay

Neutrophils were isolated from the SP as previously described, and 200,000 cells/well were plated in a 96-well round bottom plate for 1 hour at 37°C in RPMI (Thermo Fisher Scientific) + 10% FBS (Thermo Fisher Scientific) + 1% penicillin/streptomycin (Thermo Fisher Scientific). Media were then removed, and the ROS-reactive dye 2′,7′-dichlorofluorescin diacetate (Sigma-Aldrich) was added at a final concentration of 10 μg/mL in PBS for 30 minutes at 37°C. Phorbol 12-myristate 13-acetate at a final concentration of 1 μg/mL was used to stimulate ROS production. At the end of the experiment, cells were harvested, stained with a live/dead dye, and analyzed by flow cytometry.

In vitro T Cell–Killing Assay

CD8 T cells were isolated from the SP of NP-E7LP–vaccinated mice as previously described and cocultured at a 1:1 ratio with growth arrested H16sc-IS1 cancer cells (previously treated with 20 μg/mL mitomycin C) for 21 days in the presence of IL-2 (15 ng/mL) and IL-7 (10 ng/mL) to select and expand tumor-reactive CD8 T cells. The cancer cell feeder layer was replaced on day 10. Neutrophils were isolated from the SP as previously described. For *in vitro* T cell–killing assays, 7.5×10^4 H16sc-IS1 cancer cells were labelled with CFSE, seeded in a 96-well flat bottom plate, and cocultured for 24 hours with tumor-reactive CD8 T cells and neutrophils at a 1:4:4 ratio in the presence of IL-2 (10 ng/mL). Cocultured cells were harvested 24 hours later, stained with a viability dye (LIVE/DEAD Fixable Violet Dead Cell Stain Kit, Invitrogen), and analyzed by flow cytometry to assess cancer cell death.

Flow Cytometry

Single-cell suspensions of the BM, SPs or tumors were blocked with anti-mouse CD16/32 (BioLegend, Cat#101302) for 15 minutes on ice. Live/dead staining was performed using fixable viability stain kits (LIVE/DEAD Fixable Red Dead Cell Stain Kit, LIVE/DEAD Fixable Aqua Dead Cell Stain Kit, or LIVE/DEAD Fixable Yellow Dead Cell Stain Kit, Invitrogen) for 15 minutes on ice. For surface staining, cells were incubated with antibodies diluted in FACS buffer on ice for 30 minutes. E7-specific CD8 T cells were identified by staining with a tetramer recognizing the HPV16 E7 peptide 49 to 57 presented by H2Db (generated by the department of Oncology UNIL CHUV, University of Lausanne, Switzerland) on ice for 30 minutes. To perform intracellular immunostaining, mice were treated with 250 μg brefeldin A for 6 hours prior to euthanasia. Cells were fixed and permeabilized with the Foxp3/Transcription Factor Staining Buffer Set (Thermo Fisher Scientific) according to the manufacturer's instructions. Intracellular staining was carried out in Perm/Wash buffer overnight at 4°C. After staining, cells were washed and resuspended in FACS buffer. The following antibodies were used: Ly6G-PacB (BioLegend, Cat# 127611, RRID: AB_1877212), CD3-BV510 (BioLegend, Cat# 100353, RRID: AB_2565879), CD3-FITC (Thermo Fisher Scientific, Cat# 11-0031-85, RRID: AB_464883), CD3-PerCP-Cy5.5 (Thermo Fisher Scientific, Cat# 45-0031-82, RRID: AB_1107000), CD3-PE-Cy7 (Thermo Fisher Scientific, Cat# 25-0031-82, RRID: AB_469572), CD3-PE-Cy5 (Thermo Fisher Scientific, Cat# 15-0031-63, RRID: AB_468688), CD19-BV510 (BioLegend, Cat# 115546, RRID: AB_2562137), CD19-PE-Cy5 (BioLegend, Cat# 115510, RRID: AB_313645), NKp46-BV510 (BioLegend, Cat# 137623, RRID: AB_2563290), CCR2-BV605 (BD Biosciences, clone 475301), CD64-BV711 (BioLegend, Cat# 139311, RRID: AB_2563846), CD103-BV785 (BioLegend, Cat# 121439, RRID: AB_2800588), SiglecF-AF488 (BioLegend, Cat# 155523, RRID: AB_2890713), Ly6C-PerCP-Cy5.5 (Thermo Fisher Scientific, Cat# 45-5932-82, RRID: AB_2723343), PD1-PE (Thermo Fisher Scientific, Cat# 12-9981-83, RRID: AB_466291), F4/80-PE-Cy5 (BioLegend, Cat# 123110, RRID: AB_893486), CD11b-PE-Cy7 (Thermo Fisher Scientific, Cat# 25-0112-81, RRID: AB_469587), CD11b-PE-Cy5 (Thermo Fisher Scientific, Cat# 15-0112-81, RRID: AB_468713), CD11b-PacB (BioLegend, Cat# 101223, RRID: AB_755985), CD11b-BV510 (BioLegend, Cat# 101245, RRID: AB_2561390), PDL1-APC (BioLegend, Cat# 124311, RRID: AB_10612935), CD45-AF700 (BioLegend, Cat# 103127, RRID: AB_493714), CD45-APC-Cy7 (BioLegend, Cat# 103115, RRID: AB_312980), CD45-APC (BD Biosciences, Cat# 559864, RRID: AB_398672), CD11c-APC-Cy7 (BioLegend, Cat# 117323, RRID: AB_830646), CD11c-PE-Cy5 (Thermo Fisher Scientific, Cat# 15-0114-82, RRID: AB_468717), SiglecH-BV650 (BD Biosciences, clone 440c), iNOS-AF488 (Thermo Fisher Scientific, Cat# 53-5920-80, RRID: AB_2574422), MHCII-PE (eBiosicence, clone M5/114.15.2), MHCII-BV650 (BioLegend, Cat# 107641, RRID: AB_2565975), Egr2-APC (Thermo Fisher Scientific, Cat# 17-6691-82, RRID: AB_11151502), B220-PerCP-Cy5.5 (Thermo Fisher Scientific, Cat# 45-0452-80, RRID: AB_906234), B220-PE-Cy5 (Thermo Fisher Scientific, Cat# 15-0452-82, RRID: AB_468755), CD8-PacO (Thermo Fisher Scientific, Cat# MCD0830, RRID: AB_10376311), CD8-PE-Cy7 (BioLegend, Cat# 100721, RRID: AB_312760), CD8-PE-Cy5 (BioLegend, Cat# 100709, RRID: AB_312748), CD4-APC-eF780 (Thermo Fisher Scientific, Cat# 47-0041-82, RRID: AB_11218896), CD4-PE-Cy5 (Thermo Fisher Scientific, Cat# 15-0041-83, RRID: AB_468696), FoxP3-PE-Cy7 (Thermo Fisher Scientific, Cat# 25-5773-80, RRID: AB_891554), CD62L-FITC (BioLegend, Cat# 104405, RRID: AB_313092), CD44-APC-eF780 (Thermo Fisher Scientific, Cat# 47-0441-82, RRID: AB_1272244), KLRG1-PE (BioLegend, Cat# 138407, RRID: AB_10574005), CD127-BV421 (BioLegend, Cat# 135027, RRID: AB_2563103), Ki67-PacB (BioLegend, Cat# 652422, RRID: AB_2564490), TNFa-FITC (Thermo Fisher Scientific, Cat# 11-7321-82, RRID: AB_465418), Gzmb-PE (Thermo Fisher Scientific, Cat# 12-8898-82, RRID: AB_10870787), IFNg-APC (BioLegend, Cat# 505810, RRID: AB_315404), Gr1-PE-Cy5 (Thermo Fisher Scientific, Cat# 15-5931-82, RRID: AB_468813), NK1.1-PE-Cy5 (BioLegend, Cat# 108716, RRID: AB_493590), Ter119-PE-Cy5 (Thermo Fisher Scientific, Cat# 15-5921-82, RRID: AB_468810), c-Kit-APC (Thermo Fisher Scientific, Cat# 17-1171-82, RRID: AB_469430), Sca-1-biotin (Thermo Fisher Scientific, Cat# 13-5981-82, RRID: AB_466834), CD34-FITC (Thermo Fisher Scientific, Cat# 11-0341-82, RRID: AB_465021), and FcγR-PE (BD Biosciences, Cat# 553145, RRID: AB_394660). Fluorophore-conjugated streptavidin was used to detect biotinylated antibodies: SA-APC-Cy7 (BioLegend, Cat# 405208). The compensation was performed using OneComp eBeads (Invitrogen). Samples were run on a BD LSR Fortessa, Gallios (Beckman Coulter), CytoFLEX S (Beckman Coulter), or CytoFLEX LX (Beckman Coulter) cytometer, and the data were processed with the FlowJo (RRID: SCR_008520) v10.7.1 software and GraphPad Prism (RRID: SCR_002798) v9.

Immunofluorescence Staining of Mouse Tumors

Harvested mouse tissues were fixed in 4% paraformaldehyde overnight, embedded in paraffin, and sectioned using a microtome (Leica). Antigen retrieval was performed in a citrate buffer (pH = 6.0) in a water bath at 95°C for 20 minutes, followed by 0.3% H_2O_2 treatment for 10 minutes at room temperature. Primary antibodies were incubated in blocking buffer (5% normal donkey serum and 2% BSA) at 4°C overnight. Chicken anti-keratin 14 (BioLegend, Cat# 906004, RRID: AB_2616962; 1:500), rat anti-Ly6G (BioLegend, Cat# 127602, RRID: AB_1089180; 1:100), and rabbit anti-CD11b (Abcam, Cat# ab133357, RRID: AB_2650514; 1:400) were used. Secondary antibodies (Alexa Fluor 488, 568, and 647; Thermo Fisher Scientific, catalog

nos. A-11006, A-11077, and A-21247) in blocking buffer were incubated at room temperature for 45 minutes. Finally, tissues were counterstained with 4',6-diamidino-2-phenylindole (DAPI) before mounting.

RNA Scope Staining of Mouse Tumors

The RNAscope Multiplex Fluorescent V2 assay (BioTtechne, Cat. No. 323110) was performed according to the manufacturer's protocol on 4-μm paraffin sections. They were hybridized with either Mm 3plex-positive control (Bio-Techne, Cat. No. 320881), 3Plex-negative control (Bio-Techne, Cat. No. 3200871), or a combination of the following probes Mm Il36b-C1 (Bio-Techne, Cat. 425231), Mm Il33-C2 (Bio-Techne, Cat. 400591-C2), and Mm Il1a-C3 (Bio-Techne, Cat. 440391-C3) at 40°C for 2 hours. The channels were revealed with TSA Opal570 (Akoya Biosciences, Cat. No. FP1488001KT) for C1, TSA Opal650 (Akoya Biosciences, Cat. No. FP1496001KT) for C2, and TSA Opal520 (Akoya Biosciences, Cat. No. FP1487001KT) for C3 diluted 1:1,500. After 30 minutes of blocking with 1% BSA, tissues were incubated with the primary antibody, rabbit anti–pan cytokeratin, (Novus, Cat# NB600-579, RRID: AB_2296858; (1:100) overnight at 4°C. After incubation with the secondary antibody, goat anti-rabbit Alexa Fluor 750 (Thermo Fisher Scientific, Cat# A-21039, RRID: AB_2535710; 1:800), tissues were counterstained with DAPI and mounted with ProLong Gold Antifade Mountant (Thermo Fisher Scientific, Cat# P36930).

RNA Isolation, Reverse Transcription, and RT-qPCR

RNA from cancer cells and bulk tumors was isolated using miRNeasy Mini Kit (Qiagen). RNA from primary or HoxB8 neutrophils was isolated using miRNeasy Micro Kit (Qiagen). All the procedures were performed according to the manufacturer's instructions. A total of 100 to 500 ng of RNA was used for cDNA synthesis using PrimeScript RT Master Mix (TaKaRa). RT-qPCR was performed using Rotor-Gene SYBR Green Master Mix (Qiagen).

Mouse Serum Preparation

Blood was collected by intracardiac punction into Eppendorf tubes and allowed to coagulate at room temperature for 30 minutes. Tubes were then centrifuged at 2,000 *g* for 10 minutes, 4°C, and serum was carefully collected without disturbing the blood clot. Serum samples were then aliquoted and frozen at −80°C until further use, avoiding repeated freeze/thaw cycles.

Mouse Cytokine Quantification

Secreted cytokines in mouse serum or cancer cell conditioned media were quantified by ELISA or LEGENDplex technologies according to the manufacturers' instructions.

IL-1α and IL-1β were quantified using the 13-plex LEGENDplex Mouse Inflammation Panel (BioLegend) or a custom LEGENDplex panel (BioLegend). IL-33 was quantified using a custom LEGENDplex panel (BioLegend), or the Mouse IL-33 ELISA Kit (RayBiotech). IL-36β was quantified using Mouse IL-36 β/IL-1F8 ELISA Kit (RayBiotech). G-CSF was quantified using Mouse G-CSF DuoSet ELISA kit (R&D Systems).

Overexpression of Triplet IL-1 Ligands in Cancer Cells

Mouse *Il1a* [ORF (NM_010554.4)], mouse *Il33* [ORF (NM_133775.3)], and mouse *Il36b* [ORF (NM_027163.4)] were overexpressed under the *EF1A* promoter in H16sc-ImP cancer cells by lentiviral transduction. Expression vectors and control constructs were custom made by VectorBuilder. Lentivirus production and p24 titration (ELISA) were performed at the Gene Therapy Core Facility, EPFL, Switzerland. Cancer cells were plated at 4×10^4 cells/well in a 24-well plate and incubated at 37°C overnight. The next day, when cells had reached 30% to 40% confluency, viral particles were added to cells (200 TU/cell) for overnight incubation at 37°C with 8 μg/mL of polybrene. The following day, media were changed and cells were allowed to recover for 48 hours before antibiotic selection was initiated with puromycin (2 μg/mL for *Il1a*), G418 (300 μg/mL for *Il33*), or blasticidin (4 μg/mL for *Il36b*). Coexpression of the three ligands was achieved through three successive rounds of transduction.

Proliferation of H16sc-IS1 Cancer Cells

For colony formation assays, H16sc-IS1 cancer cells were resuspended in RPMI (Thermo Fisher Scientific), 10% FBS (Thermo Fisher Scientific), and 1% penicillin/streptomycin (Thermo Fisher Scientific) and in some cases supplemented with 10 μg/mL of mAb depending on the experimental condition. Cells were next seeded in six-well tissue culture plates at a density of 200 cells/well. Colony expansion of single cells were allowed to progress for 7 days at 37°C, 5% CO_2 until control cells had formed sufficiently large colonies (at least 50 cells). Culture media, supplemented or not with mAb, was replenished on day 4. On day 7, colonies were washed twice with PBS and fixed/stained with a 20% ethanol + 0.4% crystal violet (VWR) dye solution for 15 minutes at room temperature. The dye was aspirated, and wells were washed 3× with water or until all excess dye was removed. Plates were allowed to dry at room temperature. The number of colonies in each well was then counted, and data were plotted by experimental condition using GraphPad Prism (RRID: SCR_002798) *v*9.

siRNA Transfection of H16sc-IS1 Cancer Cells

H16sc-IS1 cancer cells were seeded at 200,000 cells per well into a six-well plate and transfected the next day with 20 μmol/L *siRNA* (5 μL per well, 100 pmol final) using RNAiMAX lipofectamine (5 μL per well) in OptiMEM Reduced Serum Media (Thermo Fisher Scientific, catalog no. 13778075). The transfected cells were then used for RNA extraction and RT-qPCR analysis 72 hours after transfection. siRNA constructs were purchased from Dharmacon [ON-TARGETplus predesigned siRNAs: *Il1rap* (Entrez gene 1680) SMARTpool, and nontargeting siRNAs #1 and #2].

Analysis of Blood Cell Counts anti-IL1RAP–Treated Patients

Patients with cancer from the CANFOUR trial (NCT03267316) who had received nadunolimab (CAN04) as a monotherapy ($n = 36$) were used for the analysis. Blood cell counts were measured before the treatment start (baseline) and subsequently before nadunolimab dose was given on each visit. Patients were separated based on their baseline neutrophil count, with a cutoff of 6×10^9 cell/mL, resulting in a "normal neutrophil" group (baseline $< 6 \times 10^9$ cells/mL; $n = 20$) and a "high neutrophil" group (baseline $> 6 \times 10^9$ cells/mL; $n = 16$). Neutrophil count, lymphocyte count, and the NLR were plotted as the median + 95% confidence interval. To evaluate the effect of nadunolimab treatment on blood cell counts variation, a mixed effect statistical analysis, with Dunnett's multiple comparisons, was performed (all subsequent visits compared with baseline). Statistical significance is indicated as *, $P < 0.05$; **, $P < 0.01$; ***, $P < 0.001$; and ***, $P < 0.0001$.

Human Cytokine Quantification

Single donor sera from patients with cervical cancer (pretreatment) were purchased from BioIVT. Age- and sex-matched single donor normal human serums were purchased from Innovative Research. Secreted cytokines in human serum were quantified by ELISA or LEGENDplex technologies according to the manufacturers' instructions. IL-1α was quantified using Human IL-1 α ELISA Kit (Raybio). IL-1β was quantified using Human IL-1β

ELISA Kit (Raybio). IL-33 was quantified using Human IL-33 ELISA Kit (Raybio). IL-36β was quantified using Human IL-36β (IL-1 F8) ELISA Kit (Raybio). G-CSF was quantified using Human G-CSF ELISA Kit (Raybio). CXCL1, CXCL5, IL-8, and CCL2 were quantified using the 13-plex LEGENDplex HU Proinflam. Chemokine Panel 1 (BioLegend).

Statistics

Statistical analyses were carried out using GraphPad Prism (RRID: SCR_002798) v9. Data are reported as the mean ± SEM, unless otherwise stated in the figure legends. *P* values are reported in the figures or figure legends and were assessed using the unpaired Mann–Whitney test to compare the means of two groups or one-way and two-way ANOVA for multiple group comparisons, unless otherwise stated. For survival analyses, the log-rank (Mantel–Cox) test was performed. Statistical significance is indicated as *, $P < 0.05$; **, $P < 0.01$; ***, $P < 0.001$; and ****, $P < 0.0001$.

10× Genomics Single-Cell Gene Expression Sample Processing and Sequencing

The BM, SP, blood and dysplastic ear skin of HPV mice ($n = 3$), the cervical tumor of HPV-E_2 mice ($n = 3$), and control tissues from H2b mice ($n = 3$) were used to generate single-cell suspensions as described previously. Cells were loaded into the 10× Genomics Chromium platform. Samples were processed following the manufacturer's protocol using 10× Genomics Next GEM Single Cell 5′ Kit v2 and then sequenced on an Illumina HiSeq4000 platform. Cellranger (version 6.0.1; ref. 74) was used to map FASTQ files to the mouse genome (refdata-gex-mm10-2020-A). Count tables were then opened in R (v. 4.2.0), and Seurat (v. 4.1.0) was used for downstream analysis. Only genes with a minimum of 10 cells expressing the gene were selected. Moreover, only cells expressing at least 200 genes and maximum 6,000 genes were selected (3,000 genes for the blood), with this last point in order to remove doublets. To exclude dying cells, a maximum of 20% (10% for the blood) of mitochondrial content was accepted. Data were log-normalized and scaled on the 4,000 most variable features using the variance-stabilizing method, and principal component analysis (PCA) was performed on those variable features. The Uniform Manifold Approximation and Projection (UMAP) was obtained on the first 30 PCs (cutoff was obtained using the elbow-plot method). The shared nearest neighbor (SNN) graph was obtained using default parameters, and resolutions between 0.1 and 0.8 were tested. Finally, a resolution of 0.15 (0.25 for the skin and 0.1 for the blood) was chosen to annotate the broad clusters.

Characterization of PANs

Data Integration. After selecting neutrophils (by using s100a9 expression) in the blood, BM, and SP, cells were further annotated using SingleR (RRID: SCR_023120; 1.0.1), and the reference from Zilionis and colleagues (27) was used to remove cells that would not coherently be annotated as neutrophils. Moreover, cells that were contaminated by erythrocyte gene expression in the blood were removed (starting from a number of 22,238 cells to 19,689 cells after removal). Then, the 2,000 variable features of those cells were calculated. An integration using Seurat's CCA method was performed on the 15 first PCs using the organ (BM, SP, or blood) as batch. Then, the 15 first PCs were used for a UMAP projection on the integrated object.

Neutrotime Score. A list of marker genes for "early" and "late" neutrotime was retrieved from Grieshaber-Bouyer and colleagues (24) and used with the UCell (v 1.3.1; ref. 75) AddModuleScore_UCell algorithm to produce a score per cell of the ranking of the signatures.

Clustering and Annotation. Using the SNN graph from Seurat on the first 15 dimensions and using a resolution of 0.05, clusters of neutrophils were obtained and further annotated as prePAN, PAN-1, and PAN-2 based on marker gene expression.

Characterization of Mouse TANs

Clustering. After selecting neutrophils (by clustering) in mouse cervical carcinomas, the cells were further annotated using SingleR (RRID: SCR_023120; 1.0.1) from Zilionis and colleagues (27) to remove cells that would not coherently be annotated as neutrophils. Then, 2,000 variable features were selected using the VST method, and PCA was performed followed by UMAP, which was obtained on the first 20 PCs (cutoff obtained using the elbow-plot method). The SNN graph was obtained using default parameters, and a resolution of 0.4 was chosen.

Pseudotime. Neutrophils from the K14HPV16/H2b mice samples of cervix and blood were used.

A STACAS (2.2.1) integration was performed using the location slot (blood or cervix) for the integration. A pseudotime analysis was performed using Slingshot (v.1.8.0; ref. 76), and the DimPlot was colorcoded using the pseudotime scale generated by Slingshot.

Gene Signature Scores. Using UCell (v 1.3.1), a score was generated for an MDSC signature based on genes from Alshetaiwi and colleagues (26), as well as an N5 signature based on genes from Zilionis and colleagues (27) with a relative value of at least 1.5. The mouse MDSC signature is composed of the following genes: *Wfdc17*, *Ifitm1*, *Asprv1*, *Plscr1*, *Clec4e*, *Il1b*, and *Pla2g7*. The mouse N5 signature is composed of the following genes: *Gstm1*, *Ccl3*, *Cd63*, *Lgals3*, *Hcar2*, *Hmga1*, *Spp1*, *Gas2l3*, *Slc31a2*, *Ctsb*, and *Lgmn*.

Characterization of Human TANs

scRNA-seq data from three studies have been reanalyzed and grouped to create a human cervical cancer scRNA-seq atlas. Tumor samples from the Guo and colleagues (21) publication, tumor samples before treatment from the Dai and colleagues (22) publication, as well as samples from the Li and colleagues (23) publication were reanalyzed. Data were integrated using reciprocal principal component analysis (RPCA) on the datasets in Seurat (v. 5.0.0). With a resolution of 0.3 on the first 20th integrated reciprocal principal components (RPCs), clusters have been annotated and neutrophils retrieved. Three samples had less than 10 neutrophils and were removed for further analysis. After finding variable genes using Seurat, scaling, and PCA, integration was again performed on the datasets. Resolution 0.1 was chosen for highlighting the major hTAN populations on the 20 first RPCs. Using UCell (v 1.3.1), a score was generated for a human MDSC signature based on genes from Veglia and colleagues (25), as well as a human N5 signature based on genes from Zilionis and colleagues (27) with a relative cutoff of 1. The human MDSC signature is composed of the following genes: *CD84*, *STAT1*, *STAT3*, *STAT6*, *IRF1*, *S100A8*, *S100A9*, *ANXA1*, *CXCL1*, *CXCL2*, *CXCR1*, *CXCR2*, *TREM1*, *PTGS2*, *ARG1*, *ARG2*, *TGFB1*, *IL6*, *CSF1*, *IL1B*, *CEACAM8*, *ITGAM*, *CXCL8*, and *VEGFA*. The human N5 signature is composed of the following genes: *PI3*, *SPINK1*, *MT1G*, *FNIP2*, *IL3RA*, *CSTB*, *LGALS3*, *CAST*, *PLPP3*, *SLPI*, *AC015912.3*, *TPRA1*, *GPR84*, *CSF1*, *CCL3*, *SNAPC1*, *TNFSF15*, *RMND5A*, *CCDC93*, *GNPDA1*, *ATP6V1C1*, *NPC1*, *RHEB*, *GBE1*, *TGM3*, *APLP2*, *TGM2*, *DARS*, *ATP6V1F*, *USF2*, *TMEM251*, *CNST*, *UQCRC2*, *BNIP3L*, *SEC22B*, *TRGC2*, *CCL20*, *IRAK1*, *ZNF438*, *ID2*, *JUN*, *C12orf49*, *TPI1*, and *TRIM33*.

CellChat

CellChat (v. 1.6.1) and its curated database of ligands and receptors, subselected for secreted signaling pathway, were used to evaluate on cells from the bone BM and the cervix or from the SP and the

cervix of K14HPV16/H2b mice. In both cases, an integration was first performed using Seurat's FindIntegrationAnchors on 30 dimensions to determine anchors. The data were integrated using Seurat on 30 dimensions, and PCA and UMAP were then performed using 30 PCs.

Serum Proteomic Analysis

Proteomic analysis of glycocaptured proteins from HPV and H2b mouse serum ($n = 4$) was performed by the ETH PHRT Swiss Multi-Omics Center (http://smoc.ethz.ch).

Sample Preparation. Solid-phase extraction of N-linked glycoproteins in serum samples was performed in a multiwell format as previously described (77–79) using an automated liquid handling system (Thermo Versette; ref. 79). Glycoproteins were bound to tip columns (Thermo Disposable Automation Research Tips) filled with resin (Bio-Rad, Affi-Gel Hydrazine resin) using coupling buffer (100 mmol/L sodium acetate buffer and 1 mol/L NaCl, pH 5.5) and aniline as a catalyst. Nonglycoproteins were washed off the resin with urea buffer (8 mol/L urea and 0.4 mol/L ammonium bicarbonate, pH 8.0). Reduction and alkylation of captured glycoproteins was performed with 0.5 mol/L of 10 mmol/L tris(2-carboxyethyl) phosphine hydrochloride and 132 mmol/L iodoacetamide. Tryptic digestion took place overnight at 37°C. To remove nonglycopeptides, washing steps were performed before harvesting N-linked glycopeptides with PNGase F (NEB). Eluted samples were desalted by C18 clean-up (The Nest Group) and dried using a centrifugal vacuum concentrator (Labconco CentriVap).

Mass Spectrometry Measurements. For mass spectrometry (MS) measurements, peptide samples were reconstituted in 3% acetonitrile and 0.1% formic acid in HPLC-grade water, and 1 µg of sample was loaded onto an EASY-nano-HPLC system (EASY-nLC 1200, Thermo Fisher Scientific) equipped with reverse-phase column (75 µm ID) packed in-house with a 15 cm stationary phase (Reprosil-Pur C18-AQ 1.9 µm, 200 Å, Dr. Maisch). The HPLC was coupled to a QExactive HF-X Quadrupole-Orbitrap MS System (Thermo Fisher Scientific) equipped with a nanoelectrospray ion source (Thermo Fisher Scientific). Peptides were eluted from the column with a 40-minute gradient of 5% to 24% B (80% ACN, 0.1% formic acid) followed by a 6-minute gradient from 24% to 36% B and a 4-minute gradient from 24% to 60%. The MS was operated in a data-dependent mode with MS1 resolution at 60,000 and a scan range between 350 to 1,650 m/z. The maximum injection time was set to 45 ms, and the AGC target was 3e6. Precursor ions were fragmented using collision-induced dissociation at 27% normalized collision energy with an MS2 resolution of 15,000. The AGC target was 1e5, isolation width was 1.3 m/z, and maximum IT was 22 ms. The loop count was set to 12. Selected precursors were excluded from fragmentation for 15 seconds

Data Analysis and Visualization. For data analysis, RAW data files were converted to mzML using MSconvert. Fragment ion spectra were searched with COMET (v27.0) against UniProtKB (RRID: SCR_004426; Swiss-Prot, Homo sapiens, release January 2018) containing common MS contaminants and standards. The precursor mass tolerance was set to 20 ppm. Search parameters were semi-tryptic with carbamidomethylation as the fixed modification for cysteines. Oxidation of methionine and deamidation of asparagine were set as variable modifications. Probability scoring was performed with the Trans-Proteomic Pipeline (v4.6.2) using PeptideProphet (RRID: SCR_000274). Peptides with an error rate ≤1% were selected for quantification. Peptide identifications were further filtered for the presence of the consensus NXS/T sequence with concurrent deamidation (+0.98 Da) at asparagines. Nonconflicting peptides were used in Progenesis QI (Nonlinear Dynamics) for label-free MS1-based quantification (80).

Serum Quantitative Cytokine Array

K14HPV16/H2b and FVBN/H2b mouse serum ($n = 4$) were analyzed using the Mouse Cytokine Array Q640 (RayBio) according to the manufacturer's instructions, allowing us to quantitatively measure 640 mouse cytokines.

Identification of SIS Candidates

Using the proteomic and cytokine array data, circulating soluble factors with a positive fold change in K14HPV16/H2b serum (compared with FVBN/H2b) were first selected. Associated genes were retrieved, scRNA-seq datasets from dysplastic skin and cervical tumors were interrogated, and genes expressed in both tissues from K14HPV16/H2b mice were retained. Based on the NicheNet network, genes encoding for proteins that are not considered as ligands were removed. Finally, the list of receptors corresponding to each ligand in the NicheNet network was retrieved, obtained on the url "https://zenodo.org/record/3260758/files/lr_network.rds," and used to interrogate scRNA-seq datasets from the BM and SP. Ligands for which at least one associated receptor was expressed in more than 10% of the cells of a given cell type in either the BM or SP were retained, resulting in a list of 93 candidate ligands (Supplementary Table S1). A receptor score per ligand was then generated in the BM and SP using UCell (v 1.3.1) and used for generating the heatmap presented in Supplementary Fig. S2D.

SAveRUNNER

SAveRUNNER (37), a network-based drug-repurposing tool that prioritize drug candidates by assessing relationships between drug targets and disease-associated proteins or genes, was used with the following input: (i) the list of drug–target interactions provided by the algorithm, as well as (ii) the selected panel of CIN genes from the phenopedia file provided by the algorithm. Drugs were ranked based on network-based similarity measures and associated P value.

NicheNet Analyses

Pseudobulk gene expression was created per sample and cell type in the BM and SP using aggregateAcrossCells from the scuttle package (v. 1.0.4). Differential gene expression was then performed between K14HPV16/H2b and FVBN/H2b samples, in all the cell types, by running the edgeR (RRID: SCR_012802; v. 3.32.1) pipeline (81). More specifically, the filterByExpr function was used to remove lowly expressed genes, after which genes were normalized with the TMM normalization, dispersion was estimated, and glmQLFit and glmQLFTest were then used for finding differentially expressed genes. Adjusted P-values were obtained using the Benjamini–Hochberg method. The predict_ligand_activities from the nichenetR package (v. 1.1.1; ref. 40) was used to find pearson correlation scores between the list of targets from the candidate ligands (the 93 previously curated list of genes), obtained using the ligand–target matrix provided in the NicheNet pipeline, and the list of differentially expressed genes per cluster obtained above. Heatmaps were produced using the ComplexHeatmap (RRID: SCR_017270) package (v. 2.15.1; ref. 82).

Bulk RNA-Seq of Neutrophils and Cancer Cells

Cell Preparation. Neutrophils were isolated from the BM, SP, and tumor of H16sc-IS1 tumor–bearing mice treated with anti-IL-1RAP ($n = 4$) or matching IC ($n = 4$) for 7 days. Neutrophil isolation was performed on single-cell suspensions using mouse Anti-Ly-6G UltraPure MicroBeads (Miltenyi Biotec) according to the manufacturer's instructions. Total RNA was isolated using miRNeasy Micro Kit (Qiagen) according to the manufacturer's instructions. Control and ILs-OE H16sc-ImP cancer cells and H16sc-IS1 cancer cells were

cultured in RPMI (Thermo Fisher Scientific), 10% FBS (Thermo Fisher Scientific), and penicillin/streptomycin (100 U/mL penicillin and 100 μg/mL streptomycin; Thermo Fisher Scientific). Total RNA from cancer cells was isolated using miRNeasy Mini Kit (Qiagen) according to the manufacturer's instructions.

Bulk RNA-Seq. RNA quality was assessed using the TapeStation 4200 (Agilent) to confirm their integrity. Libraries for mRNA-seq were prepared with the Stranded mRNA Ligation method (Illumina) according to manufacturer's instructions, starting from 60 ng RNA (neutrophils) and 900 ng RNA (cancer cells). Libraries, all bearing unique dual indexes, were subsequently loaded at 100 pmol/L on a Novaseq 6000 flow cell (Illumina) and sequenced according to the manufacturer's instructions, yielding pairs of 60 nucleotides reads.

Bioinformatics. Mapping and quantification were performed with STAR (RRID: SCR_004463) and Salmon (nf-core/rnaseq version 3.12.0) on the mouse genome mm10 with reverse strand setting and default parameters. Raw counts were normalized using the TMM method from edgeR (RRID: SCR_012802; v.4.0.16) and Voom from limma (RRID: SCR_010943; v.3.58.1; ref. 83). Genes with average TPM < 1 (neutrophils), TPM < 0.78 (cancer cells), or average counts <5 per sample were filtered out. Uncharacterized genes, predicted genes, and pseudogenes were removed to keep a matrix of counts with n = 11,838 genes for neutrophils and n = 11,813 for cancer cells. Differential expression between groups was computed with limma (RRID: SCR_010943; lmFit and eBayes). Pathway enrichment was computed with clusterProfiler (RRID: SCR_016884; v.4.10.1) using the Gene Ontology biological process geneset collection from r (v.7.5.1) and gene set enrichment analysis with 100,000 permutations to obtain P values. Single-sample scores were computed with the combined z-score method in the hacksig package (v0.1.2; ref. 84) using specific gene signatures. P values were adjusted with the Benjamini–Hochberg test which controls for the FDR.

SIS Signature. The top 200 genes enriched in triplet-IL-OE-H16sc-ImP cancer cells (compared with Ctrl H16sc-ImP cancer cells) were selected and cross-filtered using genes coding for the initial 93 candidate ligands, resulting in a 10-gene list used as an SIS signature.

Human Protein Atlas Analysis

Transcript expression levels were summarized per gene in 7,932 samples from 17 different cancer types. The data are based on The Human Protein Atlas version 23.0 and Ensembl (RRID: SCR_002344) version 109. FPKM expressions were averaged through all samples from a cancer type.

Unsupervised Clustering of TCGA Transcriptome Data

RNA counts and associated clinical information of the TCGA data were downloaded using the TCGAbiolinks package (v 2.18.0). After merging the logCPM data of only the tumor samples, scaling was performed through all samples per gene, and the heatmap was generated using ComplexHeatmap (RRID: SCR_017270) package (v 2.15.1).

Survival Analyses of TCGA Datasets

Survival Based on the NtoT Ratio. CESC gene expression data were downloaded using the TCGAbiolinks (v 2.18.0) legacy version, and only primary tumor expression was selected. The MCPcounter method (v 1.2.0) was used to estimate the amounts of neutrophils and T cells in those sample. The NtoT ratio was calculated using a pseudocount of 2 for both estimates to avoid negative values when calculating the ratio and dividing one by the other.

Survival Based on the SIS Signature. Using UCell (v 1.3.1), a score was generated in all tumor samples for the 10-gene signature and used for segregating samples into the lower and upper quartiles, or neither. We also evaluated the segregation of the samples into upper and lower groups using the surv_cutpoint function of the survminer package (v 0.4.9), with a minimum of 25% of the tumors in each group, referred to as the machine learning cutoff in Fig. 4C and Supplementary Fig. S4D. The Kaplan–Meier curves were obtained using the survival package (v. 3.2.7) for fitting, and the survminer package was used for plotting the curves.

Correlation analyses in TCGA datasets

MCPcounter (v. 1.2.0) was used to estimate the abundance of neutrophils in the different samples. A scatterplot was drawn using ggplot2 (RRID: SCR_014601; v. 3.4.4), and a smoothing function using a linear model in ggsmooth function was used to estimate the linear relationship between neutrophil abundance and the SIS signature score, generated by averaging the scaled expression of the 10-gene signature.

Data Availability

The K14-HPV16/H2b GEMM is available from the European Mouse Mutant Archive, (https://www.infrafrontier.eu/emma/), as strain Tg(KRT14-HPV16)wt1Dh with an European Mouse Mutant Archive ID of EM:15289; the congenic FVBN/H2b strain necessary for breeding is also available (EM:15300). The three described GEMM-derived cancer cell lines, as well as the HoxB8 neutrophil progenitors and SCF-producing CHO cells, are available from the corresponding author. The anti-IL1RAP nadunolimab surrogate antibody (mNadunolimab, clone 3A9) is available from Cantargia AB upon reasonable request to the corresponding author. The CANFOUR clinical trial (NCT03267316) data analyzed for this publication are not publicly available due to patient privacy requirements, but anonymized datasets analyzed during the current study are available upon reasonable request to the corresponding author. Sequencing data (scRNA-seq and bulk RNA-seq) generated in this study are deposited in the Gene Expression Omnibus (RRID: SCR_005012) with the submission number GSE268241.

Authors' Disclosures

E. Jaensson Gyllenbäck reports personal fees from Cantargia AB outside the submitted work; in addition, E. Jaensson Gyllenbäck has a patent for "mAbs to IL1RAP" pending and licensed to Cantargia AB and is an employee at Cantargia AB. D. Liberg reports personal fees from Cantargia AB outside the submitted work; in addition, D. Liberg has a patent for "Novel antibodies and uses thereof" issued, a patent for "Anti-IL1RAP antibodies" issued, and a patent for "Anti-Il1RAP antibody composition" issued and is employed at Cantargia AB. K. Homicsko reports grants from ROCHE/Genentech, Bristol Myers Squibb, Tolremo, Merck Sharp Dohme, Boehringer Ingelheim, DOPPL SA, and Parithera SA and personal fees from Incyte outside the submitted work. D. Hanahan reports no financial support from Cantargia AB, or other potential conflicts of interest, during the conduct of the study. No disclosures were reported by the other authors.

Authors' Contributions

M. Lecointre: Conceptualization, data curation, formal analysis, investigation, methodology, writing–original draft, writing–review and editing. **J. Guillot:** Conceptualization, data curation, formal analysis, investigation, methodology, writing–original draft, writing–review and editing. **R. Marcone:** Data curation, formal analysis, investigation, methodology. **D. Ozdoganlar:** Investigation. **M. Cayatte:** Investigation, Master's Internship Research. **E. Jaensson Gyllenbäck:** Resources, provided anti-mouse-IL1RAP antibody and anonymized

data from a clinical trial involving anti-human-IL1RAP. **D. Liberg:** Resources, provided anti-mouse-IL1RAP antibody and anonymized data from a clinical trial involving anti-human-IL1RAP. **N. Fournier:** Data curation, formal analysis, investigation, methodology. **K. Homicsko:** Investigation (scRNA-sequencing). **D. Hanahan:** Conceptualization, supervision, funding acquisition, writing–original draft, writing–review and editing.

Acknowledgments

We thank: E. Drori, M. Munier, M. Alexandre-Gaveta, and S. André-Baflast from the Hanahan laboratory for expert technical assistance; M. Pittet (University of Geneva and the Ludwig Institute for Cancer Research, Lausanne Branch) for comments on the project, scientific discussions, and insightful comments on the manuscript; T. Kaufmann (University of Bern) for the Hoxb8 and SCF-producing CHO cell lines; J. Sordet-Dessimoz (from the HCF at EPFL) for the RNAscope staining and scientific advice; T. Zwahlen (from the SIB in the Agora Center) for the SAveRUNNER analysis; and B. Schneider (from the PTBTG at EPFL) for lentiviral production. Proteomics datasets were generated by the ETH PHRT Swiss Multi-Omics Center. ETH PHRT SMOC is in part supported by the strategic focus area Personalized Health and Related Technologies of the ETH Domain. The anti-mouse-IL1RAP antibody was a gift from Cantargia AB, Sweden. This study benefited also from the CPG, GECF, BIOP, and FCCF technology core facilities of the School of Life Sciences at EPFL and the AIVC, CIF, SIB, and FCF facilities at the Agora Translational Cancer Research Center. The research was variously supported by an Advanced Grant from the European Research Council, a Project Grant the Swiss National Science Foundation, core support from the Ludwig Institute for Cancer Research (New York/Zurich), and by philanthropic grants from the Cancera and Paulsson Foundations (Lund) and from Goran Grosskopf (Lund), all administered by the CHUV Foundation, Lausanne.

Note

Supplementary data for this article are available at Cancer Discovery Online (http://cancerdiscovery.aacrjournals.org/).

Received March 2, 2025; revised April 2, 2025; accepted April 3, 2025; posted first April 27, 2025.

REFERENCES

1. Hanahan D, Weinberg RA. Hallmarks of cancer: the next generation. Cell 2011;144:646–74.
2. Pan Y, Yu Y, Wang X, Zhang T. Tumor-associated macrophages in tumor immunity. Front Immunol 2020;11:583084.
3. Jaillon S, Ponzetta A, Di Mitri D, Santoni A, Bonecchi R, Mantovani A. Neutrophil diversity and plasticity in tumour progression and therapy. Nat Rev Cancer 2020;20:485–503.
4. van Weverwijk A, de Visser KE. Mechanisms driving the immunoregulatory function of cancer cells. Nat Rev Cancer 2023;23:193–215.
5. de Visser KE, Joyce JA. The evolving tumor microenvironment: from cancer initiation to metastatic outgrowth. Cancer Cell 2023;41:374–403.
6. Nøst TH, Alcala K, Urbarova I, Byrne KS, Guida F, Sandanger TM, et al. Systemic inflammation markers and cancer incidence in the UK Biobank. Eur J Epidemiol 2021;36:841–8.
7. Hiam-Galvez KJ, Allen BM, Spitzer MH. Systemic immunity in cancer. Nat Rev Cancer 2021;21:345–59.
8. Galliverti G, Tichet M, Domingos-Pereira S, Hauert S, Nardelli-Haefliger D, Swartz MA, et al. Nanoparticle conjugation of human papillomavirus 16 E7-long peptides enhances therapeutic vaccine efficacy against solid tumors in mice. Cancer Immunol Res 2018;6:1301–13.
9. Galliverti G, Wullschleger S, Tichet M, Murugan D, Zangger N, Horton W, et al. Myeloid cells orchestrate systemic immunosuppression, impairing the efficacy of immunotherapy against HPV+ cancers. Cancer Immunol Res 2020;8:131–45.
10. Allen BM, Hiam KJ, Burnett CE, Venida A, DeBarge R, Tenvooren I, et al. Systemic dysfunction and plasticity of the immune macroenvironment in cancer models. Nat Med 2020;26:1125–34.
11. LaMarche NM, Hegde S, Park MD, Maier BB, Troncoso L, Le Berichel J, et al. An IL-4 signalling axis in bone marrow drives pro-tumorigenic myelopoiesis. Nature 2024;625:166–74.
12. Smith-McCune K, Zhu YH, Hanahan D, Arbeit J. Cross-species comparison of angiogenesis during the premalignant stages of squamous carcinogenesis in the human cervix and K14-HPV16 transgenic mice. Cancer Res 1997;57:1294–300.
13. Arbeit JM, Howley PM, Hanahan D. Chronic estrogen-induced cervical and vaginal squamous carcinogenesis in human papillomavirus type 16 transgenic mice. Proc Natl Acad Sci U S A 1996;93:2930–5.
14. Coussens LM, Hanahan D, Arbeit JM. Genetic predisposition and parameters of malignant progression in K14-HPV16 transgenic mice. Am J Pathol 1996;149:1899–917.
15. Coussens LM, Tinkle CL, Hanahan D, Werb Z. MMP-9 supplied by bone marrow–derived cells contributes to skin carcinogenesis. Cell 2000;103:481–90.
16. Giraudo E, Inoue M, Hanahan D. An amino-bisphosphonate targets MMP-9–expressing macrophages and angiogenesis to impair cervical carcinogenesis. J Clin Invest 2004;114:623–33.
17. Pietras K, Pahler J, Bergers G, Hanahan D. Functions of paracrine PDGF signaling in the proangiogenic tumor stroma revealed by pharmacological targeting. PLoS Med 2008;5:e19.
18. Erez N, Truitt M, Olson P, Arron ST, Hanahan D. Cancer-associated fibroblasts are activated in incipient neoplasia to orchestrate tumor-promoting inflammation in an NF-kappaB-Dependent manner. Cancer Cell 2010;17:135–47.
19. Pere H, Montier Y, Bayry J, Quintin-Colonna F, Merillon N, Dransart E, et al. A CCR4 antagonist combined with vaccines induces antigen-specific CD8+ T cells and tumor immunity against self antigens. Blood 2011;118:4853–62.
20. Daniel D, Meyer-Morse N, Bergsland EK, Dehne K, Coussens LM, Hanahan D. Immune enhancement of skin carcinogenesis by CD4+ T cells. J Exp Med 2003;197:1017–28.
21. Guo C, Qu X, Tang X, Song Y, Wang J, Hua K, et al. Spatiotemporally deciphering the mysterious mechanism of persistent HPV-induced malignant transition and immune remodelling from HPV-infected normal cervix, precancer to cervical cancer: integrating single-cell RNA-sequencing and spatial transcriptome. Clin Transl Med 2023;13:e1219.
22. Dai D, Pei Y, Zhu B, Wang D, Pei S, Huang H, et al. Chemoradiotherapy-induced ACKR2+ tumor cells drive CD8+ T cell senescence and cervical cancer recurrence. Cell Rep Med 2024;5:101550.
23. Li C, Wu H, Guo L, Liu D, Yang S, Li S, et al. Single-cell transcriptomics reveals cellular heterogeneity and molecular stratification of cervical cancer. Commun Biol 2022;5:1208.
24. Grieshaber-Bouyer R, Radtke FA, Cunin P, Stifano G, Levescot A, Vijaykumar B, et al. The neutrotime transcriptional signature defines a single continuum of neutrophils across biological compartments. Nat Commun 2021;12:2856.
25. Veglia F, Sanseviero E, Gabrilovich DI. Myeloid-derived suppressor cells in the era of increasing myeloid cell diversity. Nat Rev Immunol 2021;21:485–98.
26. Alshetaiwi H, Pervolarakis N, McIntyre LL, Ma D, Nguyen Q, Rath JA, et al. Defining the emergence of myeloid-derived suppressor cells in breast cancer using single-cell transcriptomics. Sci Immunol 2020;5:eaay6017.
27. Zilionis R, Engblom C, Pfirschke C, Savova V, Zemmour D, Saatcioglu HD, et al. Single-cell transcriptomics of human and mouse lung cancers reveals conserved myeloid populations across individuals and species. Immunity 2019;50:1317–34.e10.
28. Pfirschke C, Engblom C, Gungabeesoon J, Lin Y, Rickelt S, Zilionis R, et al. Tumor-promoting ly-6g+ SiglecFhigh cells are mature and long-lived neutrophils. Cell Rep 2020;32:108164.

29. Pahler JC, Tazzyman S, Erez N, Chen Y-Y, Murdoch C, Nozawa H, et al. Plasticity in tumor-promoting inflammation: impairment of macrophage recruitment evokes a compensatory neutrophil response. Neoplasia 2008;10:329–39.
30. Affara NI, Ruffell B, Medler TR, Gunderson AJ, Johansson M, Bornstein S, et al. B cells regulate macrophage phenotype and response to chemotherapy in squamous carcinomas. Cancer Cell 2014;25:809–21.
31. Medler TR, Murugan D, Horton W, Kumar S, Cotechini T, Forsyth AM, et al. Complement C5a fosters squamous carcinogenesis and limits T cell response to chemotherapy. Cancer Cell 2018;34:561–78.e6.
32. Jin S, Guerrero-Juarez CF, Zhang L, Chang I, Ramos R, Kuan C-H, et al. Inference and analysis of cell-cell communication using CellChat. Nat Commun 2021;12:1088.
33. Sawant KV, Sepuru KM, Lowry E, Penaranda B, Frevert CW, Garofalo RP, et al. Neutrophil recruitment by chemokines Cxcl1/KC and Cxcl2/MIP2: role of Cxcr2 activation and glycosaminoglycan interactions. J Leukoc Biol 2021;109:777–91.
34. Alcaide P, Auerbach S, Luscinskas FW. Neutrophil recruitment under shear flow: it's all about endothelial cell rings and gaps. Microcirculation 2009;16:43–57.
35. Pliyev BK. Anti-adhesive proteins and resolution of neutrophil-mediated inflammation. Immunobiology 2013;218:1085–92.
36. Martin KR, Wong HL, Witko-Sarsat V, Wicks IP. G-CSF - a double edge sword in neutrophil mediated immunity. Semin Immunol 2021;54:101516.
37. Fiscon G, Conte F, Farina L, Paci P. SAveRUNNER: a network-based algorithm for drug repurposing and its application to COVID-19. PLoS Comput Biol 2021;17:e1008686.
38. Garlanda C, Mantovani A. Interleukin-1 in tumor progression, therapy, and prevention. Cancer Cell 2021;39:1023–7.
39. Yeoh WJ, Vu VP, Krebs P. IL-33 biology in cancer: an update and future perspectives. Cytokine 2022;157:155961.
40. Browaeys R, Saelens W, Saeys Y. NicheNet: modeling intercellular communication by linking ligands to target genes. Nat Methods 2020;17:159–62.
41. Huang Q-T, Man Q-Q, Hu J, Yang Y-L, Zhang Y-M, Wang W, et al. Prognostic significance of neutrophil-to-lymphocyte ratio in cervical cancer: a systematic review and meta-analysis of observational studies. Oncotarget 2017;8:16755–64.
42. Hansen N, Peña-Martínez P, Skoog P, Reinbach K, Hansen FC, Larsson FS, et al. Blocking IL1RAP on cancer-associated fibroblasts in pancreatic ductal adenocarcinoma suppresses IL-1-induced neutrophil recruitment. J Immunother Cancer 2024;12:e009523.
43. Singhal S, Bhojnagarwala PS, O'Brien S, Moon EK, Garfall AL, Rao AS, et al. Origin and role of a subset of tumor-associated neutrophils with antigen-presenting cell features in early-stage human lung cancer. Cancer Cell 2016;30:120–35.
44. Wu Y, Ma J, Yang X, Nan F, Zhang T, Ji S, et al. Neutrophil profiling illuminates anti-tumor antigen-presenting potency. Cell 2024;187:1422–39.e24.
45. Coffelt SB, Kersten K, Doornebal CW, Weiden J, Vrijland K, Hau C-S, et al. IL-17-producing γδ T cells and neutrophils conspire to promote breast cancer metastasis. Nature 2015;522:345–8.
46. Mellman I, Chen DS, Powles T, Turley SJ. The cancer-immunity cycle: indication, genotype, and immunotype. Immunity 2023;56:2188–205.
47. Esmaily M, Masjedi A, Hallaj S, Nabi Afjadi M, Malakotikhah F, Ghani S, et al. Blockade of CTLA-4 increases anti-tumor response inducing potential of dendritic cell vaccine. J Control Release 2020;326:63–74.
48. Salvatori E, Lione L, Compagnone M, Pinto E, Conforti A, Ciliberto G, et al. Neoantigen cancer vaccine augments anti-CTLA-4 efficacy. NPJ Vaccines 2022;7:15.
49. Hanahan D. Hallmarks of cancer: new dimensions. Cancer Discov 2022;12:31–46.
50. Hanahan D, Michielin O, Pittet MJ. Convergent inducers and effectors of T cell paralysis in the tumour microenvironment. Nat Rev Cancer 2025;25:41–58.
51. De Palma M, Hanahan D. Milestones in tumor vascularization and its therapeutic targeting. Nat Cancer 2024;5:827–843.
52. Garner H, de Visser KE. Immune crosstalk in cancer progression and metastatic spread: a complex conversation. Nat Rev Immunol 2020;20:483–497.
53. Swanton C, Bernard E, Abbosh C, André F, Auwerx J, Balmain A, et al. Embracing cancer complexity: hallmarks of systemic disease. Cell 2024;187:1589–616.
54. Hanahan D, Monje M. Cancer hallmarks intersect with neuroscience in the tumor microenvironment. Cancer Cell 2023;41:573–80.
55. Serrano B, Brotons M, Bosch FX, Bruni L. Epidemiology and burden of HPV-related disease. Best Pract Res Clin Obstet Gynaecol 2018;47:14–26.
56. Bray F, Laversanne M, Sung H, Ferlay J, Siegel RL, Soerjomataram I, et al. Global cancer statistics 2022: GLOBOCAN estimates of incidence and mortality worldwide for 36 cancers in 185 countries. CA Cancer J Clin 2024;74:229–63.
57. Kenter GG, Welters MJP, Valentijn ARPM, Lowik MJG, Berends-van der Meer DMA, Vloon APG, et al. Vaccination against HPV-16 oncoproteins for vulvar intraepithelial neoplasia. N Engl J Med 2009;361:1838–47.
58. Welters MJP, Kenter GG, De Vos Van Steenwijk PJ, Löwik MJG, Berends-van Der Meer DMA, Essahsah F, et al. Success or failure of vaccination for HPV16-positive vulvar lesions correlates with kinetics and phenotype of induced T-cell responses. Proc Natl Acad Sci U S A 2010;107:11895–9.
59. Yan F, Cowell LG, Tomkies A, Day AT. Therapeutic vaccination for HPV-mediated cancers. Curr Otorhinolaryngol Rep 2023;11:44–61.
60. Monk BJ, Sill MW, McMeekin DS, Cohn DE, Ramondetta LM, Boardman CH, et al. Phase III trial of four cisplatin-containing doublet combinations in stage IVB, recurrent, or persistent cervical carcinoma: a gynecologic Oncology group study. J Clin Oncol 2009;27:4649–55.
61. Walsh RJ, Tan DSP. The role of immunotherapy in the treatment of advanced cervical cancer: current status and future perspectives. J Clin Med 2021;10:4523.
62. Watkins DE, Craig DJ, Vellani SD, Hegazi A, Fredrickson KJ, Walter A, et al. Advances in targeted therapy for the treatment of cervical cancer. J Clin Med 2023;12:5992.
63. Gulhati P, Schalck A, Jiang S, Shang X, Wu C-J, Hou P, et al. Targeting T cell checkpoints 41BB and LAG3 and myeloid cell CXCR1/CXCR2 results in antitumor immunity and durable response in pancreatic cancer. Nat Cancer 2023;4:62–80.
64. Quail DF, Amulic B, Aziz M, Barnes BJ, Eruslanov E, Fridlender ZG, et al. Neutrophil phenotypes and functions in cancer: a consensus statement. J Exp Med 2022;219:e20220011.
65. Ridker PM, MacFadyen JG, Thuren T, Everett BM, Libby P, Glynn RJ, et al. Effect of interleukin-1β inhibition with canakinumab on incident lung cancer in patients with atherosclerosis: exploratory results from a randomised, double-blind, placebo-controlled trial. Lancet 2017;390:1833–42.
66. Tan DSW, Felip E, de Castro G, Solomon BJ, Greystoke A, Cho BC, et al. Canakinumab versus placebo in combination with first-line pembrolizumab plus chemotherapy for advanced non–small-cell lung cancer: results from the CANOPY-1 trial. J Clin Oncol 2024;42:192–204.
67. Garon EB, Lu S, Goto Y, De Marchi P, Paz-Ares L, Spigel DR, et al. Canakinumab as adjuvant therapy in patients with completely resected non–small-cell lung cancer: results from the CANOPY-A double-blind, randomized clinical trial. J Clin Oncol 2024;42:180–191.
68. Paz-Ares L, Goto Y, Wan-Teck Lim D, Halmos B, Chul Cho B, Cobo M, et al. Canakinumab in combination with docetaxel compared with docetaxel alone for the treatment of advanced non-small cell lung cancer following platinum-based doublet chemotherapy and immunotherapy (CANOPY-2): a multicenter, randomized, double-blind, phase 3 trial. Lung Cancer 2024;189:107451.
69. Monteran L, Ershaid N, Scharff Y, Zoabi Y, Sanalla T, Ding Y, et al. Combining TIGIT blockade with MDSC inhibition hinders breast cancer bone metastasis by activating antitumor immunity. Cancer Discov 2024;14:1252–75.

70. Hirosue S, Kourtis IC, Van Der Vlies AJ, Hubbell JA, Swartz MA. Antigen delivery to dendritic cells by poly(propylene sulfide) nanoparticles with disulfide conjugated peptides: cross-presentation and T cell activation. Vaccine 2010;28:7897–906.
71. Rincon-Restrepo M, Mayer A, Hauert S, Bonner DK, Phelps EA, Hubbell JA, et al. Vaccine nanocarriers: coupling intracellular pathways and cellular biodistribution to control CD4 vs CD8 T cell responses. Biomaterials 2017;132:48–58.
72. Van Der Vlies AJ, O'Neil CP, Hasegawa U, Hammond N, Hubbell JA. Synthesis of pyridyl disulfide-functionalized nanoparticles for conjugating thiol-containing small molecules, peptides, and proteins. Bioconjug Chem 2010;21:653–62.
73. Kamala T. Hock immunization: a humane alternative to mouse footpad injections. J Immunol Methods 2007;328:204–14.
74. Zheng GXY, Terry JM, Belgrader P, Ryvkin P, Bent ZW, Wilson R, et al. Massively parallel digital transcriptional profiling of single cells. Nat Commun 2017;8:14049.
75. Andreatta M, Carmona SJ. UCell: robust and scalable single-cell gene signature scoring. Comput Struct Biotechnol J 2021;19:3796–8.
76. Street K, Risso D, Fletcher RB, Das D, Ngai J, Yosef N, et al. Slingshot: cell lineage and pseudotime inference for single-cell transcriptomics. BMC Genomics 2018;19:477.
77. Chen J, Shah P, Zhang H. Solid phase extraction of N-linked glycopeptides using hydrazide tip. Anal Chem 2013;85:10670–4.
78. Zhang H, Li X, Martin DB, Aebersold R. Identification and quantification of N-linked glycoproteins using hydrazide chemistry, stable isotope labeling and mass spectrometry. Nat Biotechnol 2003;21:660–6.
79. Zila N, Eichhoff OM, Steiner I, Mohr T, Bileck A, Cheng PF, et al. Proteomic profiling of advanced melanoma patients to predict therapeutic response to anti-PD-1 therapy. Clin Cancer Res 2024;30:159–75.
80. Sobotzki N, Schafroth MA, Rudnicka A, Koetemann A, Marty F, Goetze S, et al. HATRIC-based identification of receptors for orphan ligands. Nat Commun 2018;9:1519.
81. Robinson MD, McCarthy DJ, Smyth GK. edgeR: a bioconductor package for differential expression analysis of digital gene expression data. Bioinformatics 2010;26:139–40.
82. Gu Z, Eils R, Schlesner M. Complex heatmaps reveal patterns and correlations in multidimensional genomic data. Bioinformatics 2016;32:2847–9.
83. Ritchie ME, Phipson B, Wu D, Hu Y, Law CW, Shi W, et al. Limma powers differential expression analyses for RNA-sequencing and microarray studies. Nucleic Acids Res 2015;43:e47.
84. Carenzo A, Pistore F, Serafini MS, Lenoci D, Licata AG, De Cecco L. hacksig: a unified and tidy R framework to easily compute gene expression signature scores. Bioinformatics 2022;38:2940–2.